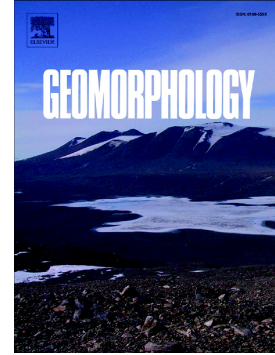# Accepted Manuscript

Flow resistance, sediment transport, and bedform development in a steep gravel-bedded river flume

Marisa C. Palucis, Thomas P. Ulizio, Brian Fuller, Michael P. Lamb

Please cite this article as: Marisa C. Palucis, Thomas P. Ulizio, Brian Fuller, Michael P. Lamb , Flow resistance, sediment transport, and bedform development in a steep gravel-bedded river flume. Geomor (2018), doi:10.1016/j.geomorph.2018.08.003

Title: Flow resistance, sediment transport, and bedform development in a steep gravel-bedded river flume

Authors: Marisa C. Palucis*[1,2], Thomas P. Ulizio[1], Brian Fuller[1], and Michael P. Lamb[1]

Author Affiliations: [1]California Institute of Technology, Division of Geological and Planetary Sciences, 1200 E. California Blvd., Pasadena, CA 91125; [2]Dartmouth College, Department of Earth Sciences, Hanover, NH 03755

*Corresponding Author: Marisa C. Palucis, marisa.c.palucis@dartmouth.edu

Highlights:

- Flow resistance increased with shallow flow, bedforms, and high sediment transport intensity

- Downstream and upstream migrating alternate bars developed on bed slopes up to 20%

- Transition to upper plane bed coincided with development of concentrated sheetflow

Abstract: Quantifying flow resistance and sediment transport rates in steep streams is important for flood and debris flow prediction, habitat restoration, and predicting how mountainous landscapes evolve. However, most studies have focused on low gradient rivers and the application of this work is uncertain for steep mountain streams where surface flows are shallow and rough, subsurface flows are not negligible, and there is form-drag from bed- and channel-forms that differs from those in low gradient rivers. To evaluate flow resistance relations and sediment transport rates for steep channel beds, experiments were conducted using a range of water discharges and sediment transport rates in a 12 m long recirculating flume with bed slopes of 10%, 20%, and 30%, and a bed of nearly uniform natural gravel. Flow resistance for planar beds and beds that developed bedforms match empirical models that account for bedload-dependent roughness. Some bedforms were atypical for natural rivers at these bed slopes, such as

stepped alternate bars and upstream migrating alternate bars. Total flow resistance increased with decreasing particle submergence and energetic sediment transport and drag on bedforms. Using linear stress partitioning to calculate bed stresses due to grain resistance alone, sediment flux relations developed for lower gradient rivers perform well overall, but they overestimate fluxes at 20% and 30% gradients. Based on previous theory, mass failure of the bed, which did not occur, was predicted for the highest Shields stresses investigated at 20% and 30% bed slopes; instead a concentrated layer, four to ten particle diameters deep, of highly concentrated granular sheetflow was observed.

Keywords: flow resistance, sediment transport, mountain streams, alternating bars, sheetflow, debris flow

1. Introduction

Steep mountain streams are an important component of the river network, as they provide aquatic habitat (Church, 2002), are conduits for sediment delivered to lower gradient channels (Milliman and Syvitski, 1992; Yager et al., 2012), and they comprise much of the channel network in mountainous regions (Shreve, 1969; Stock and Dietrich, 2003). Understanding steep stream hydraulics and sediment transport is therefore important for flood and debris flow prediction and mitigation, channel engineering and restoration, and landscape evolution (Buffington et al., 2004; Jakob et al., 2005; Takahashi, 2007; Rickenmann and Recking, 2011). However, most studies on river processes have focused on lower gradient rivers and flume studies ($S < 1\%$, where S is the tangent of the bed slope angle, θ), leaving uncertainty about whether relations developed for flow resistance and bedload fluxes can be applied to steeper channels (Scheingross et al., 2013; Schneider et al., 2015). For example, it has been suggested that flow resistance coefficients (C_f), which relate bed shear velocity ($u^* = \sqrt{\tau_b/\rho}$, where τ_b is

the bed stress and ρ is the density of water) to the depth-averaged water flow velocity (U) (i.e., $C_f = u_*^2/U^2$), in steep streams are much greater than empirical models predict (Bathurst, 1985; Wilcox et al., 2006; Ferguson, 2007; Rickenmann and Recking, 2011). This has been hypothesized to be due to increased form drag caused by pressure differentials around immobile clusters of grains, boulders, bedforms or woody debris (Wilcox et al., 2006; Yager et al., 2007; Ferguson, 2012). Alternatively, it has been shown that flow resistance increases in shallow, rough flows due to changes in the velocity profile near a rough bed (Lamb et al., 2017a,b). Similarly, sediment transport rates are thought to be different in steep streams, as the presence of immobile (or rarely mobile) boulders, particle clusters, and channel forms, such as step-pool sequences, may stabilize sediment (Church et al., 1998; Chin and Wohl, 2005; Yager et al., 2007; Zimmermann et al., 2010; Prancevic and Lamb, 2015). In addition, increased form drag may reduce available shear stress for entraining and transporting sediment, leading models to under-predict critical shear stresses for initial motion of the bed (τ_c^*) and over-predict sediment fluxes (Rickenmann, 1997; Yager et al., 2007; Mueller et al., 2008; Nitsche et al., 2011; Schneider et al., 2015). Lower lift coefficients and reduced turbulent intensities in steep, shallow flows may also cause reduced sediment transport rates (Lamb et al., 2008, 2017a, b).

Although bed- and channel-forms affect flow resistance and sediment transport (Hassan and Reid, 1990; Aberle and Smart, 2003; Nitsche et al., 2011), bedform stability regimes are still largely unknown for mountain streams (Wohl and Merritt, 2005; Zimmermann et al., 2010; Buffington and Montgomery, 2013; Palucis and Lamb, 2017). Field observations suggest that different channel morphologies can be attributed to distinct ranges in bed slope (Buffington and Montgomery, 2013). For example, Montgomery and Buffington (1997) showed that channel state changes from alternate bars to plane bed (or the absence of channel- or bed-forms) to steps

3

and pools to cascade morphology with increasing channel bed slope. This is in contrast, however, to more mechanistic theoretical and experimental investigations into the formation of specific channel states, where variables such as the channel width (W) to flow depth (H) ratio or the Froude number ($Fr = U/(gH)^{0.5}$, where g is the acceleration due to gravity), not bed slope, are shown to control channel state (Colombini et al., 1987; Grant et al., 1990; Montgomery et al., 2003; Church and Zimmermann, 2007). Combining field data and theory, Palucis and Lamb (2017) showed that these controlling variables co-vary systematically with bed slope, but predicting which state will emerge under a given set of conditions is still unclear.

The difficulty in observing active sediment transport in steep streams, combined with the lack of data on steep river hydrodynamics under a wide range of flow conditions, has led some to conduct flume experiments aimed at measuring flow resistance and sediment fluxes at steep bed slopes ($1\% < S \leq 20\%$) (Smart and Jäggi, 1983; Bathurst et al., 1984; Cao, 1985; Graf et al., 1987; Rickenmann, 1990; Recking, 2010). Cao (1985) collected hydraulic data for slopes ranging from 1 to 9% and relative submergence (defined as the ratio of the flow depth to the bed roughness height, k_s, which often scales with grain diameter, D) between 1.3 and 14, and showed that the resistance coefficient increased with decreasing H/D. Smart and Jaggi (1983) and Rickenmann (1990) produced data for steeper bed slopes (up to $S = 20\%$) and a relative submergence of ~4, and saw increases in flow resistance with increasing sediment transport. Recking (2006) collected data in the same slope range as Cao (1985), but at higher bed shear stresses, in order to isolate the effect of bedload transport on C_f at a given H/D. In most previous work, the sediment bed was maintained at planar or near-planar conditions (i.e., no bedforms) and the flow depth was often deeper than a sediment diameter (i.e., relative submergence > 1). Mizuyama (1977) and Bathurst et al. (1984) conducted some of the few flume experiments on

4

20% bed slopes, with bed stresses high enough to develop bedforms, namely anti-dunes and alternating bars, and relative submergence as low as ~0.7. Mizuyama (1977) did not observe differences in flow resistance coefficients between a plane bed and one with alternating bars, but he did see slight increases in C_f with the onset of thalweg sinuosity. He also found that flow velocity did not change significantly with the onset of sediment transport. Lamb et al. (2017a) explored the effect of steep bed slopes (up to $S = 30\%$) and shallow flows (submergence down to 0.1) on flow resistance over a fixed, planar bed, but in the absence of sediment transport. They found that flow resistance matched observations in natural steep streams, despite the lack of bed- or channel-forms, suggesting that grain drag can account for much of the observed flow resistance in steep natural streams.

Another complicating factor in understanding very steep rivers is whether fluvial processes (where fluid-particle interactions result in rolling, saltation, or dilute suspensions of grains (Shields, 1936)), or mass flow processes dominate in the range of $10\% < S < 30\%$ in natural channels. The model proposed by Takahashi (1978) for in-channel bed failure assumes that when applied shear stresses (due to parallel seepage and surface flow) overcome resisting stresses within a granular bed at some depth, δ, particles above δ move together (*en masse*). Prancevic et al. (2014) showed through flume experiments that there exists a critical slope (S_c), defined as the slope above which in-channel failures occur prior to any bedload transport. They suggest that mass failure of channel beds might occur at slopes lower than the critical slope if the dimensionless bed stress, or the Shields stress ($\tau^* = \frac{\tau_b}{(\rho_s - \rho)gD}$, where ρ_s is the sediment density), is substantially higher than the critical value for fluvial transport (e.g., Shields stresses approaching one), based on the model of Takahashi (1978). While very few studies have investigated this regime, Smart and Jaggi (1983) observed that for $S = 20\%$, the mode of transport transitioned at

5

high Shields stresses ($\tau^* \sim 0.69$) such that it became difficult to distinguish between bedload and suspended load. Mizuyama (1977) also found that for S=20% and $\tau^* \to 1$, the mode of transport changed, such that the upper portion of the bed began to 'creep', which he referred to as an 'immature' debris flow, and others have described as a debris flood (Hungr et al., 2014). While these studies suggest that a transport transition may occur at high τ^*, the observations and data are sparse, especially for $S > 20\%$.

There is a need to acquire flow resistance and sediment flux data at steep slopes ($S \geq$ 10%) under high bed stresses in order to test whether fluvial or debris flow transport processes dominate (*sensu* Prancevic et al., 2014), and to determine if commonly used flow resistance models (Ferguson, 2007; Recking et al., 2008) and sediment flux models (Recking, 2010; Schneider et al., 2015) are broadly applicable to very steep channels. To address this need, a series of steep flume experiments were conducted in the Earth Surface Dynamics Laboratory at the California Institute of Technology. A subset of data from these experiments appears in a companion paper, Palucis et al. (2018), which focused specifically on the development of sheetflow at high Shields numbers, the structure of particle velocities within sheetflows, and how these flows differ from sheetflow occurring in low gradient systems or dry granular flow. In this contribution we present new data on the development of bedforms, flow resistance and sediment transport across the bedload-to-sheetflow transition. Our major objectives were to (1) determine whether debris flows could initiate via mass failure of the bed under uniform water flow conditions, (2) characterize the evolution and morphology of bedforms on steep slopes, (3) determine how these bedforms affect flow resistance and sediment fluxes, and (4) test flow resistance and sediment flux relations. The methods and experimental setup are discussed in Section 2, and the flow resistance and sediment flux data, as well as a detailed characterization of

6

the bed state under each equilibrium flow condition, are presented in Section 3. Section 4 discusses how bed states differ from low-sloping rivers and affect flow resistance and sediment fluxes, and Section 5 is a summary of our findings.

2. Experimental setup and methods

As testing the bed failure model of Takahashi (1978) and Prancevic et al. (2014) was a major goal, a large flume width-to-grain diameter ratio ($W_{fl}/D_{84} = 29.5$, where D_{84} is the grain size for which 84% of the grains are smaller) was chosen to suppress the development of granular force chains that might cause grain jamming with the side walls, which could inhibit bed failure (Jop et al., 2005; Prancevic et al., 2018). This condition also likely suppressed the formation of step pools (Church and Zimmermann, 2007). A thick sediment bed, relative to the flow depth, was chosen to allow for a wide range of possible bed failure-plane depths (Takahashi, 1978; Prancevic et al., 2014). This experimental setup is unlike some natural mountain stream beds that have a thin veneer of large boulders over a relatively narrow bedrock channel, pieces of coarse woody debris, and other roughness elements (Montgomery and Buffington, 1997). These attributes were deliberately not included in our experiments to focus on conditions for bed failure in order to isolate the effect of channel bed slope and Shields stress on bedform development and sediment fluxes in a simplified system. The experimental setup is more directly analogous to mountain channels in arid landscapes, especially those that have recently experienced a large input of sand or fine gravel from landsliding and bank failures (Coe et al., 2008; Berger et al., 2011; McCoy et al., 2012), or following wildfire where the destruction of vegetation 'dams' on hillslopes results in an influx of fine sediment (Cannon et al., 2008; Lamb et al., 2013). The experiments conducted under high bed stresses are also relevant for large flood events and

associated hazards, when sediment transport rates are extreme and macro-scale topography (e.g., boulder steps) are washed out (Turowski et al., 2009).

All experimental runs were conducted in a 12 m long, 0.18 m wide, re-circulating, tilting flume (Fig. 1a). The channel had one smooth glass wall and one smooth aluminum wall. Seventy experiments were conducted (Table S1) at three different bed slopes with surface discharges (Q_{sur}) ranging from 1 x 10^{-4} to 21.7 x 10^{-4} m^3/s at S = 10%, 0.5 x 10^{-4} to 54.9 x 10^{-4} m^3/s at S = 20%, and 2.9 x 10^{-4} to 9.4 x 10^{-4} m^3/s at S = 30% (Table S1). The surface discharge was defined as the total discharge (Q) minus the subsurface discharge (Q_{sub}); the subsurface discharge ranged from 15% to 94% of the total inlet discharge for different experimental flow conditions owing to the thick (~20 cm) bed of permeable gravel, allowing for parallel seepage flow (Takahashi, 1978; Prancevic et al., 2014, 2018). The flume slope was measured to within 0.1% accuracy by measuring the flume bed elevation at its upstream and downstream end with vertical tapes ($\pm$ 2 mm accuracy). The flume slope was used as the bed slope under planar flow conditions, but for cases where alternate bars formed, the bed slope was calculated using the sinuous thalweg length rather than the flume length. Bed slopes for alternate bar conditions were all within < 2% of the flume slope (e.g., for a flume slope of S = 10%, the bed slope ranged from 9.98 to 10.02%).

The experiments were conducted with natural river gravels that were derived from an alluvial fan deposit emanating from the San Gabriel Mountains near Irwindale, CA. The gravels had a median grain size (D_{50}) of 5.4 mm and a D_{84} of 6.5 mm (Fig. 1b). Following the Folk and Ward (1957) classification scheme, the gravels had a sorting coefficient $\sigma = (\phi_{84} - \phi_{16})/4 + (\phi_{95} - \phi_5)/6.6= 0.3$ (where $\phi_i = \log_2 D_i/D_o$, and D_o is a reference diameter equal to 1 mm), such that they are very well sorted. The sediment size used was chosen to be large enough to have turbulent particle Reynolds numbers under planar bed conditions ($Re_p = U*D/\nu > 3$ x 10^2, where ν is the

8

kinematic viscosity of water), which is the case for gravel and coarser sediment in steep channels (Trampush et al., 2014) and therefore provides an analog by dynamic scaling (Lamb et al., 2015). For each experiment, the initial sediment bed was hand screeded to ensure that the initial bed conditions were uniform and planar throughout the entirety of the flume's test section (i.e., the center 10 m of the flume). A single layer of grains was fixed to the bottom of the flume to prevent sliding along the floor of the flume, and to force bed failure, should it occur, to develop within the granular bed as predicted by Takahashi (1978). To measure S_c, we performed experiments identical to Prancevic et al. (2014) except using gravel from our experiments and a flume width of 18 cm; S_c was found to be ~41%, indicating that initial sediment motion occurred by bed failure, which generated debris flows, for $S \geq 41\%$. Porosity (η) of the gravels was measured by comparing the material density to the bulk density and was found to have a value of 0.4. The dry angle of repose (ϕ_d) was measured using a tilting chute with the same width as the flume channel. A planar, 20 cm thick bed was screeded and the chute was slowly tilted until a granular avalanche occurred. To test for possible buoyancy or lubrication effects, these tests were also performed with the small chute completely submerged in static water. In both the dry and fully submerged cases the angle of repose was 41 ± 0.6 degrees. When the bed was partially saturated, the angle of repose (ϕ_{ps}) was 49 ± 0.6 degrees. The pocket friction angle of individual grains (ϕ_o) was measured by gluing individual particles to a board, placing loose individual grains on the glued grains, and tilting the board until the test particle dislodged. For 100 trials, the average pocket friction angle was 62 ± 14 degrees, similar to measurements made with other natural gravels in the field and lab (Miller and Byrne, 1966; Johnston et al., 1998; Prancevic et al., 2014; Prancevic and Lamb, 2015).

Prior to the start of each experiment, the initial bed was scanned at sub-mm vertical accuracy and 1 mm spatial resolution along the channel width and 5 mm spatial resolution down channel using a Keyence laser distance meter attached to a motorized cart. The top of the bed was defined as the average elevation from these scans (z=0, Fig. 1c), which ranged from 20.6 to 21.4 cm above the impermeable flume floor. Once the bed was screeded and scanned, the water discharge into the flume was increased until the entire sub-surface of the bed was saturated (i.e., the water level was raised to z=0), and the pump discharge was taken to be the subsurface discharge. The pump discharge was measured with two in-line magnetic flow meters, both of which were verified using standard salt dilution methods (Hongve, 1987). After the subsurface was saturated, the water and sediment discharge were increased to the desired settings for the experiment (Table S1). Sediment was recirculated with conveyers, and the flume was monitored visually for sediment flux input adjustments needed to maintain grade. Following previous work, all measurements were taken once equilibrium conditions were reached (Bathurst et al., 1984; Iseya and Ikeda, 1987; Lisle et al., 1991; Recking, 2010). Equilibrium was defined by a lack of aggradation or degradation of the bed along the test section, a steady alluvial bed slope, and when the sediment flux entering the flume equaled that exiting the flume. Sediment fluxes out of the flume were calculated from weighed samples at the exit of the test section. A Massa ultrasonic probe attached to the motorized cart, which had sub-mm accuracy in the vertical direction, was used to periodically measure the water surface topography during each run, which was used to ensure the system was maintaining a steady slope. For a given experiment, either the inlet conditions (altering roughness) or the outlet conditions (altering the weir height or weir porosity) were adjusted to maintain uniform flow conditions throughout the test section.

Along the side walls of the flume were five SLR digital cameras with a resolution of 12 pixels per centimeter after correction for minor distortion (post image processing was conducted using commercial software). At this resolution, an individual grain was ~6 pixels in diameter and therefore fully resolvable in videos and still frames. From videos, surface flow depths, the bedload layer depth, and sediment bed depths were measured at 15 to 20 locations along the test section. For some flow conditions, grains within the sediment bed were observed moving as continuous granular sheets with thicknesses (H_g) up to ten grain diameters thick, which were mapped (Fig. 1c). The solid fraction (C_b) of the sheetflow layer, as well as the static bed layer, was determined from still frames by counting the number of particles that touched the glass (n_p) in a volume $A*D_{50}$ where A ~100 cm^2; C_b for each flow condition (Table S1) was calculated using:

$$C_b \sim \frac{1.15 n_p V_p}{A D_{50}} \quad (1)$$

where V_p is the particle volume, assumed to be spherical with a diameter equal to D_{50}, and 1.15 accounts for the difference in packing between spheres and natural grains (Bridge, 1981).

Plan view movies of the experiments were taken with overhead webcams, located ~2.7 m above the surface of the sediment bed, and still frames from a SLR camera attached to the motorized cart. These images were used to document bedform evolution (e.g., bar wavelengths, dimensions, and migration velocities) through the range of flow conditions tested, and to measure the channel width, which ranged from 0.03 m to the flume width of 0.18 m.

For a given experiment, the average flow velocity was calculated following continuity ($U = Q_{sur} / HW$, assuming a rectangular channel cross section). Flow velocity was verified by either injecting dye pulses into the flow and tracking the dye front down the length of the flume or tracking foam pieces down the length of the flume. The measured velocities were within 15% of

11

the velocities calculated from continuity. All surface flows were turbulent ($Re = UH/\nu > 600$) and Froude numbers ranged from 0.4 to 1.6. To verify uniform flow conditions in the flume, the magnitude of spatial accelerations ($U\mathrm{d}U/\mathrm{d}x + g\mathrm{d}H/\mathrm{d}x$) relative to gravitational acceleration due to the sloping bed ($g\sin\theta$) were compared following Lamb et al. (2017a). For all of the experimental runs performed here, the dimensionless flow acceleration terms were less than ~17% of the gravitational term, allowing us to approximate bed stresses assuming steady and uniform flow conditions averaged over the test section (i.e., $\tau_b = \rho g R_h S$ where R_h is the hydraulic radius calculated using a side-wall correction depending on the fraction of the banks that were smooth (f_w) or alluvial ($1 - f_w$) (Vanoni and Brooks, 1957; Chiew and Parker, 1994), which changed in different experiments (Table S1).

Calculated flow resistance coefficients were compared to both H/D_{84} and R_h/D_{84} as different flow resistance models use H or R_h. In cases where sheetflow developed, H is the clear water flow depth above the bed (Fig. 1c) and does not include the sheetflow thickness (H_g). Flow resistance and bedform data were analyzed from previous flume experiments for comparison ($0.1\% \leq S \leq 20\%$; (Bathurst et al., 1984; Ikeda, 1984; Lanzoni, 2000; Recking, 2006; Lamb et al., 2017a). The data from these experiments fill in some of the major data gaps for $S = 20\%$ and 30% with active sediment transport and relative submergences near one. The relative contributions to flow resistance from grain drag, bedload transport, and bedforms were estimated by assuming that the total (i.e., measured) resistance coefficient can be linearly partitioned (Einstein and Banks, 1950; Wilcox et al., 2006; Yager et al., 2007):

$$C_f = \bar{C}_{f,grain} + \bar{C}_{f,bedload} + \bar{C}_{f,bedforms} \qquad (2)$$

where $\bar{C}_{f,grain}$ is the mean resistance coefficient from the 'no-motion' cases (where the only source of resistance is due to grain drag), $\bar{C}_{f,bedload}$ was calculated by taking the measured C_f

12

from planer bed cases with sediment transport (i.e., upper plane bed / sheetflow cases) and subtracting off the grain drag component (i.e., $\bar{C}_{f,bedload} = C_f - \bar{C}_{f,grain}$), and $\bar{C}_{f,bedforms}$ was calculated from cases with active transport and bedforms (i.e., initial motion and alternate bars cases at S=10% and S=20% where $\bar{C}_{f,bedforms} = C_f - \bar{C}_{f,grain} - \bar{C}_{f,bedload}$). To compare to the Lamb et al. (2017a) model for flow resistance of coupled surface and subsurface flow, the seepage velocity at the bed surface (u_o) was estimated using:

$$u_o = \frac{C U_{sub}}{\eta} \qquad (3)$$

where U_{sub} is the mean subsurface velocity (estimated as Q_{sub} / $H_{bed} W_{fl}$, where H_{bed} is the thickness of the sediment bed) and C is a constant that depends on the shape of the velocity profile near z=0; it was assumed here that the profile is linear and hence $C = 2$ (see discussion in Lamb et al., 2017a).

Measured critical Shields stresses for initial sediment motion were compared with several empirical and theoretical models (Miller et al., 1977; Lamb et al., 2008; Recking et al., 2008; Schneider et al., 2015; Lamb et al., 2017b), as well as field and flume data compiled by Prancevic et al. (2014). For the Lamb et al. (2008) model, a measured grain pocket friction angle (ϕ_o) of 62 degrees, a lift to drag coefficient ratio (F_L/F_D) of 0.85, a grain diameter to relative roughness of the bed (D/k_s) of 1, and a form drag correction (τ_m/τ_T, where τ_m is the shear stress spent on morphologic drag and τ_T is the total driving stress on the bed) of 0.7 was used, following Lamb et al. (2008). We also compared our data to their empirical fit, where $\tau_c^* = 0.15 S^{0.25}$. For the Lamb et al. (2017b) model, the same values as the Lamb et al. (2008) model were used, except we used the flow velocity model tested and developed in Lamb et al. (2017a), where the median drag coefficient for submerged particles ($C_{D,sub}$ in Eq. (12) in Lamb et al. (2017b)) was set to 0.4 and the median lift coefficient for well submerged particles ($C_{L,sub}$ in Eq.

13

(13) in Lamb et al. (2017b)) was set to 1. For Schneider et al. (2015), $\tau_r^* = 0.56S^{0.5}$ was used, which is their reference (or critical) Shields stress derived from total bedload transport rates, and based on the total boundary shear stress.

For each experiment, the dimensionless total sediment flux, or the Einstein number (Φ), was calculated using:

$$\Phi = \frac{q_s}{D_{50}\sqrt{RgD_{50}}} \qquad (4)$$

where R is the submerged density of quartz (i.e., 1.65) and q_s is the total volumetric transport rate per unit width. The contribution of sheetflow to the total sediment flux was estimated by measuring grain motion within the sediment bed using displacement maps. To generate these maps, successive video frames (every 1/60 s) were compared with a 6-pixel correlation window (or approximately one grain diameter) using a dense optical flow algorithm based on the Farneback algorithm (Farnebäck, 2003). From the displacement maps, downstream particle velocities at a given depth z within the bed were calculated by averaging the displacement along a row parallel to the flume bed (extending 15 cm upstream and 15 cm downstream of where a surface flow depth measurement was extracted) and dividing by the elapsed time (1/60 s). Short movie clips (order one to two seconds) extracted at the same time as flow depth measurements provided 60 to 120 frames (~60 fps) per flow condition and location, resulting in a time-averaged velocity at that location. This analysis was repeated for 10 locations in the center 3 m of the flume (each sample was taken ~ 30 cm apart), so that the final average particle velocity at a given depth within the bed was the result of both time- and space-averaging. Volumetric fluxes per unit width were estimated from the displacement maps using:

$$q_s = C_b \sum_{h=-H_g}^{h=0} U_{p,i} h_i \qquad (5)$$

14

where $U_{p,i}$ is the average particle velocity of the ith layer and h_i is the thickness of the ith layer (Fig. 1c). The flux data were compared to two empirical models, that of Recking et al. (2008) and Parker (1979), the latter of which used a constant reference τ_c*=0.03. For these models, the grain Shields stress (τ_g*) was calculated using the bed stress due to grain resistance alone (i.e., $\tau_{b,grain} = \rho \bar{C}_{f,grain} U^2$, Table S1) following Yager et al. (2012). The flux data were also compared to the Schneider et al. (2015) model, where in their model transport stage is used, defined as the ratio of the Shields stress (i.e., $\tau*$; where the total bed stress is used, i.e., $\tau_b = \rho g R_h S$) to the Schneider et al. (2015) reference Shields stress.

3. Observations

3.1. Bed characterization

For the range of bed slopes and water discharges investigated, the observed sediment transport behavior differed from that typically documented in lower gradient flume studies at similar Shields stresses. In general, it was observed that at low Shields stresses, the bed was unstable to very slight perturbations in water and sediment discharges and that due to the range of low particle submergence under which all of these experimental runs were conducted, grains in motion rarely saltated or hopped, instead they rolled. While the bed state was initially disordered at low flows for S = 10% and 20% under moderate transport rates, the beds all eventually produced regular alternating bars and pools. The bars and pools behaved differently than described for low gradient rivers as they changed from downstream migrating to upstream migrating with increasing bed slope. Lastly, with increasing Shields stress, all bedforms washed out to produce planar beds, and at S = 20% and 30%, sheetflow was observed. These observations are described in detail below.

3.1.1. No motion

15

For each bed slope, several experiments were performed where there was flume-width-spanning flow, but little to no sediment motion over the course of each experiment (~10 to 30 min). These 'no motion' cases occurred at $0.04 < \tau^* < 0.09$ and $0.6 < H/D < 1.2$ for $S=10\%$, $\tau^* < 0.1$ and $H/D = 0.7$ for $S = 20\%$, and $0.16 < \tau^* < 0.22$ and $0.7 < H/D < 1.0$ for $S = 30\%$ (See Table 1 and Table S1 for additional experimental parameters). Occasionally during these experiments, regions of the flume where the flow depth was locally deeper (due to slight variations in the bed packing based on visual inspections of the bed), led to individual grain motion over short distances and slight re-arrangements of the bed, but the bed maintained an overall planar topography.

3.1.2. Initial motion

As the Shields stresses were increased beyond 'no motion', different bed behavior was observed at each channel bed slope. Due to shallow flow and steep slopes, the sediment beds were unstable to slight perturbations in either flow or local sediment transport, such that once individual grains began to move, sediment transport rapidly increased. Thus, while referred to as 'initial motion' cases, they were quite unlike initial motion conditions observed in lower gradient flume studies (e.g., Fernandez Luque and Van Beek, 1976; Abbott and Francis, 1977) with moderate partial transport.

At $S=10\%$, initial motion conditions occurred under increasing flow conditions between $0.16 < \tau^* < 0.18$ and $2.6 < H/D < 3.2$ (Figs. 2 and 3). Under these bed stresses, slight disturbances (e.g., small fluctuations in local flow depth) throughout the flume would locally cause order 1 to 10 grains to mobilize (usually via rolling, not saltation). At these moderately steep bed slopes, the removal of these grains caused the upslope grains resting on them to also begin moving, until regularly spaced topographic lows (pools) began to emerge down the length

16

of the flume, usually along one wall. The pool widths were uniform (0.05 to 0.06 m) and tended to draw down surface water into them such that the bed surface neighboring each pool (in the cross-stream direction) did not have surface flow, and hence little transport occurred there (i.e., the bed elevation remained close to $z = 0$). These regions had the appearance of bars, but they were not depositional, rather were unsubmerged to partially submerged surfaces of the original bed. The flow exiting the pools widened, shallowed, and any entrained sediment deposited downstream of the pool, leading to near channel-width-spanning topographic highs, also bar-like in appearance, with elevations of $z>0$ (Fig. 2). In general, the sediment to build these bars was supplied from upstream by headward erosion of the pool, where individual grains were observed moving in response to seepage flow. In side-view, the bars and pools appeared to 'step' their way down the flume, resulting in a 'stepped bar' morphology similar to step pools (Fig. 3). Once this system of bars and pools was established, little sediment transport occurred, and when it did, it was mainly localized to headward erosion of the pools.

At S=20%, initial motion of the sediment occurred under increasing flow conditions between $0.13 < \tau^* < 0.26$ and $0.9 < H/D < 2.2$ (Figs. 4 and 5). At these conditions, similar to the S=10% case, once individual grains began to move, upslope neighboring grains also began to move (mostly via rolling), and the bed was unable to maintain a planar topography. Similar to the S=10% case, in the regions where grains mobilized, pools formed, but unlike the S=10% case, once these pools formed, surface flow was immediately drawn down into the pools such that little surface flow occurred elsewhere in the flume (Fig. 4). The pools were located along the side wall of the flume in a fairly narrow ($0.02 < W < 0.05$ m), straight channel. The sediment that mobilized to form the pools eventually deposited downstream, though not as much aggradation occurred as at S=10%, such that most of the bed outside of the pools was close to its initial

elevation (z=0, Fig. 5). Similar to the case at S=10%, once this system of pools was established, little to no sediment transport occurred. When sediment did move, it was mainly from seepage erosion at the upstream head of the pools.

The transition from no motion to initial motion at $S = 30\%$, which occurred at $0.22 < \tau^* < 0.26$ and $1.1 < H/D < 1.2$, differed from the other experiments in that bedform development was not observed. At this slope, when sediment began to initially move, grains within a ~0.18 m wide (i.e., flume-width spanning) and ~0.8 m long area all mobilized together and rolled downstream. These granular 'sheets' occasionally drained and stopped moving when they encountered portions of the bed that were slightly higher in elevation and therefore had shallow surface flow, due to differences in initial packing of the bed, but overall the bed maintained a planar topography.

3.1.3. Alternate bars

At both $S = 10\%$ and $S = 20\%$, the bed state produced regular cyclic alternating bars and pools, however, the bars and pools behaved differently than has been described for low gradient rivers and flume experiments (e.g., Leopold, 1982; Ikeda, 1984). A change from downstream migrating bars to upstream migrating bars was observed with increasing bed slope.

At $S = 10\%$, alternate bars formed at $\tau^* = 0.16$, $H/D = 2.4$ and $Fr = 0.9$ (Fig. 6). In this initial stage of bar formation, expansion of the pools was observed, both from increased erosion at the pool head, mostly via grain motion due to seepage flow, and lateral erosion of the bed adjacent to the pools due to fluid shear. The latter led to the formation of bars with morphologies that closely resembled those observed in lower gradient flume experiments (e.g., S=3%; Lisle et al., 1991). Due to the permeability of the gravel, water went around the bars (creating a sinuous surface flow path) and also flowed through the bars (Fig. 3a).

Under increasing Shields stresses ($0.19 < \tau^* \leq 0.22$) and $3.1 < H/D < 3.6$ at S=10%, the onset of downstream migration of the bars was observed (Fig. 6). The wavelength between bars (λ), defined as the distance between successive bar crests along the same wall of the flume, ranged from 1.3 to 2.1 m, the Froude number ranged from 0.6 to 1.6, and the flume width-to-depth ratio ranged from 7.7 to 11.5. Water flowing through the bars was able to transport partially submerged sediment across the bar surface, and these mobilized grains often mobilized nearby grains through particle collisions, resulting in the upstream boundary of the bars moving downstream. Surface flow flowing around the bars also entrained sediment, and this sediment either moved farther downstream or was re-deposited on the downstream end of the bar. The combination led to the overall downstream migration of the bars.

At $S = 20$%, alternate bars emerged at $\tau^* = 0.30$, $H/D = 2.4$, and $Fr = 1.2$. Under these conditions, increased surface flow exiting each pool was deflected towards the opposite flume wall, where the flow incised into the initial bed surface, before turning and connecting to the next downstream pool, creating a sinusoidal thalweg with alternating bars and pools (Fig. 4c). These bars differed from the alternate bars at S=10% in that they all were initially formed from a mainly erosional process (i.e., erosion of the bed to form pools and erosion of the bed between pools to establish alternating pools with bars whose tops were close to z=0). Initially, the lee faces of the bars at S=20% had slopes close to ~60% and individual moving grains were observed, likely due to a combination of the steep face and seepage flow. At the onset of bar formation, the bars had wavelengths ranging from 0.5 to 0.7 m and a flume width-to-depth ratio of 13.6.

For $\tau^* > 0.30$, $2.4 < H/D < 4.6$, and $0.5 < Fr < 0.9$ at S=20%, the bar fronts became more rounded and less steep through grain avalanching. Sediment eroded from the lee of the bar was

either transported downstream or was immediately redeposited on the upstream end of the neighboring bar. The combination of erosion on the lee side of the bar and deposition on the stoss side, resulted in bar migration upstream. This is unlike the bars at $S = 10\%$, which migrated downstream due to sediment re-deposition on the lee of the bar (Fig. 6b). With increasing τ^*, increased lateral erosion of the bar occurred, resulting in widening and shallowing of the channel, and consequently, narrowing of the bar. However, lengthening of the bars from deposition, especially on the upstream end of the bars, also occurred, such that the bars evolved towards longer wavelengths while decreasing in height (relative to the water surface) (Fig. 7a). This trend was not observed at $S=10\%$ as the bars were stable only for a very narrow range of τ^* before transitioning to plane bed (as described below).

Figure 7b compares alternate bars from our $S=10\%$ and 20% cases to alternate bars from lower gradient flume experiments. Using data compiled from Ikeda (1984), where channel bed slope ranged from $0.002 < S < 0.1$, bar wavelength is plotted as a function of channel width. Despite the changing behavior and migration directions of bars at these steep slopes, bar wavelength was ~8 channel widths.

3.1.4. Upper plane bed and sheetflow

With increasing τ^*, upper plane bed conditions developed at $S=10\%$ and sheetflow developed at $S=20\%$ and 30%. These conditions were analyzed in detail by Palucis et al. (2018) focusing on the dynamics of sheetflow, and their results are briefly summarized here.

For $S=10\%$, upper plane bed occurred at $0.22 < \tau^* < 0.26$ and $3.2 < H/D < 4.0$. The flow spanned the entire flume width (i.e., 0.18 m) and sediment transport was mainly through grains rolling, but occasionally saltation with low angle trajectories. Under plane bed conditions at this slope, almost the entire surface layer of the bed (i.e., grains at $z=0$) moved as a continuous sheet

20

that was approximately one grain diameter thick. Occasionally grains immediately below the moving layer appeared to be dragged by moving grains above, but these lower grains would often only move a few grain diameters downslope before locking up and becoming stationary again.

Upper plane bed conditions developed at $S = 20\%$ for $0.49 < \tau^* < 0.78$ and $3.5 < H/D < 5.8$. Again, the flow spanned the entire flume width, but sediment transport was observed to occur in two modes, namely a dilute bedload layer above a concentrated sheetflow layer. The sheetflow had an average concentration close that of the stationary bed ($C_b \sim 0.35$ to 0.45 in the sheetflow layer and $C_{b,bed} \sim 0.54$ to 0.6 in the static bed, Table S1), and averaged three to five grain diameters thick, where the upper grains moved faster than the lower grains.

At $S=30\%$, upper plane bed conditions occurred at $0.35 < \tau^* < 0.47$ and $1.6 < H/D < 2.2$, and similar to $S=20\%$, a dilute bedload layer was observed overriding a sheetflow layer. At this slope, the sheetflow was typically eight to ten grain diameters deep. Again, the average solids concentration within the sheetflow layer was close to that of the stationary bed ($C_b \sim 0.34$ to 0.45 in the sheetflow layer versus $C_{b,bed} \sim 0.54$ to 0.6 in the bed). In similar experiments performed at steeper slopes ($S>30\%$) with comparable gravel sizes, Prancevic et al. (2014) observed *en masse* run-away failures with well-developed granular fronts. Failure of the bed in this way was not observed under the range of τ^* investigated.

3.2. Flow resistance

For $S=10\%$, C_f decreased significantly with increasing relative submergence for the 'no motion' cases (Fig. 8). Under increasing τ^* and through the development of stepped bars to alternate bars to planar conditions, relative submergence was $2 < H/D < 4$, and changes in flow resistance did not necessarily correspond with the presence of bedforms.

21

In contrast, for S=20%, C_f changed little with increasing relative submergence for the 'no motion' and initial motion cases (Fig. 8). At higher τ^*, corresponding changes in the bed morphology from bars to planar conditions, relative submergence was $2 < H/D < 6$. For this relative submergence, the scatter can largely be explained by the development and evolution of alternating bar bedforms (Fig. 8) and the eventual transition to plane bed. There is some overlap, but overall lower C_f was observed for plane bed versus alternate bars.

For S=30%, C_f increased slightly with increasing relative submergence for the 'no motion' cases (Fig. 8), and the onset of sediment transport occurs at higher relative submergence and higher C_f. Unlike the $S = 20$% case, the onset of planar flow at relative submergence ~1 to 2 resulted in even higher C_f.

Figure 8 compares data from these experiments to the Lamb et al. (2017a) model, which accounts for the effect of non-Darcian subsurface flow through a gravel bed on the main flow (and hence on the flow resistance). This model was developed for and tested with planar, rough beds, in the absence of sediment transport, and as such, it is expected to be most applicable to "no motion" cases. When the flow velocity (u_o) at z=0 is zero (i.e., a 'no slip' condition), the Lamb et al. (2017a) model closely follows the Ferguson (2007) model. As flow through the near subsurface increases, and $u_o/u^* > 0$, the Lamb et al. (2017a) model predicts lower C_f for low H/D_{84} relative to the 'no slip' case. For these experiments, u_o/u^* ranged from 0.4 to 1.5 (See Table S1). The Lamb et al. (2017a) model for this range of u_o/u^* does well predicting flow resistance coefficients for 'no motion' cases at $S = 10$%, 20% and 30%. In contrast, the Manning-Strickler model, which was developed for deep flows over planar, rough beds, under-predicts C_f. The Manning-Strickler relationship is often used to determine grain resistance when partitioning between grain and form resistance even in steep rivers (e.g., Wilcock et al., 2009;

Schneider et al., 2015), but our results show that it can under predict grain drag by more than an order of magnitude. Neither the Lamb et al. (2017a) nor Manning-Strickler model match the data closely when there are bedforms or active sediment transport.

In Fig. 9, the same data from Fig. 8 are compared to the Ferguson (2007) and Recking et al. (2008) models, which use R_h instead of H for relative submergence. The Ferguson (2007) model, which is a good characterization of flow resistance in steep natural streams (including integrating the effect of bedforms and shallow flow depths (Rickenmann and Recking, 2011)) predicts flow resistance approximately proportional to R_h/D_{84} for very shallow, clear water flows (order of a grain diameter or less). Compared to our experiments, the Ferguson (2007) model tends to over-predict C_f for the no motion cases with low relative submergence. At higher relative submergence (i.e., $1 < R_h/D_{84} < 5$) and for cases with bedforms, Ferguson (2007) under-predicts C_f. At $1 < R_h/D_{84} < 5$, the Recking et al. (2008) model, which specifically incorporates high sediment transport rates and sheetflow (but assumes a planar bed), predicts more rapidly increasing flow resistance with increasing submergence compared to Ferguson (2007). The Recking et al. (2008) model predicts that flows with high sediment transport stages (defined as $\tau^*/\tau_c^* > 2.5$, or their domain 3 (D3), Fig. 9) will have higher flow resistance (i.e., slower velocities) than flows with equivalent depths of clear water. Our data for $S = 10\%$, 20%, and 30% where there is active sediment transport fall mostly along the high transport (D3) model, though there is scatter, especially for the non-planar bed cases. For both the S=10% and 20% data, the scatter can largely be explained by the development and evolution of alternating bar bedforms (Fig. 9) before the eventual transition to plane bed.

Figure 10a shows the geometric mean flow resistance coefficient (C_f) under different flow conditions (i.e., no motion, initial motion, bedload transport with bedforms and upper-plane

23

bed / sheetflow) for each bed slope, and Fig. 10b shows the relative contributions of grain resistance, morphologic drag due to bedforms, and sediment transport when all are present (with the exception of S=30%, which has no bedform contribution). At S=10%, flow resistance coefficients were higher for planar beds with sediment transport (C_f = 0.11) as compared to no motion cases (C_f = 0.07, Fig. 10a). Cases with bedforms at S=10%, but with only modest sediment transport, resulted in a similar C_f to the planar high sediment transport case (C_f ~ 0.1 versus 0.11). At S=10%, for cases with bedforms, stress partitioning suggests that grain resistance accounted for ~45% of the total resistance, bedforms accounted for 36%, and sediment transport accounted for 16% (Fig. 10b). The highest flow resistance at S=10% (C_f ~ 0.14) was measured for the initial motion cases, which was likely due to the proto-alternate bars that created a somewhat disorganized bed topography and a stepped topographic bed profile. For S=20%, the highest flow resistance of C_f ~ 0.35 was observed when bedforms were present with active sediment transport (Fig. 10a). Stress partitioning suggests that the relative contributions to the total flow resistance coefficient for these cases was 33%, 53%, and 14% for grain, bedform, and transport, respectively (Fig. 10b). Under upper plane bed conditions at S = 20%, flow resistance coefficients were only slightly higher than the no motion case (C_f ~ 0.16 versus 0.11), despite the sheetflow layer. For S=30%, bedforms did not develop within the flume, so the only sources of flow resistance were grain drag and sediment transport. In this case, the sheetflow layer that developed was approximately twice as thick as the sheetflow layer at S=20%, and resulted in a four-fold increase in C_f; grain resistance accounted for approximately a third of the total resistance coefficient at S = 30% (Fig. 10b).

3.3. Sediment transport

Figure 11 shows the critical Shields stress at initial sediment motion as a function of channel bed slope and comparison to several models (Miller et al., 1977; Lamb et al., 2017a, 2008; Recking et al., 2008; Schneider et al., 2015). The median critical Shields stress increases with increasing bed slope, and for a given bed slope, the critical Shields stress was higher (almost an order of magnitude higher) than the constant reference model (i.e., $\tau_c^* = 0.045$) predicted. While the Lamb et al. (2008, 2017b) empirical relation and the Recking (2008) model show the right trend with bed slope, they under-predict τ_c^*. The best fits are the Lamb et al. (2008, 2017b) models, and the Schneider et al. (2015) model, an empirical model derived from total bedload transport rates from steep streams with $D>4$ mm.

The dimensionless sediment flux (Φ) versus Shields stress data (considering grain stress only, τ_g^*) are plotted in Fig. 12a and Φ versus the transport stage (τ^*/τ_r^*) are plotted in Fig. 12b. In Fig. 12a, the Recking et al. (2008) model matched the data well, and was a slightly better fit to the data than the Parker (1979) model, which was developed for lower gradient gravel-bedded rivers, especially at high Shields numbers. Both the Parker (1979) and Recking et al. (2008) models under-predicted sediment fluxes for the S=30% cases where an intense sheetflow layer developed and over-predicted fluxes for some of the alternate bar cases. Departure from the models for these latter cases was likely due to the presence of bedforms. Figure 12b compares results from these experiments to the Schneider et al. (2015) model, which was developed using data from steep mountain streams to account for slope and macro-roughness effects. In almost all planar cases for $S \geq 10\%$, the Schneider et al. (2015) model under-predicted sediment fluxes, though less so for $S = 10\%$, but overall did slightly better than the Recking et al. (2008) or Parker (1979) models for predicting sediment fluxes when bedforms are present. The fluxes measured from the sediment trap included both dilute bedload (material transported in the surface flow,

25

$z>0$) and sheetflow, while the image analysis estimated fluxes just included material transported in the sheetflow layer (with the exception of $S=10\%$, where sheetflow was not observed, and hence the image analysis was capturing the bedload flux occurring at $z\sim0$). On average, sheetflow contributed $\sim$ 15% of the total measured flux at $S=20\%$ and ~44% at $S=30\%$.

4. Discussion

4.1. Mode of transport: fluvial versus mass flow behavior

The channel-form data from these experiments were mapped as a function of bed slope and Shields stress in the phase space proposed by Prancevic et al. (2014) (i.e., zones of no motion, fluvial sediment transport, and bed failure) in Fig. 14. For each slope investigated, there was a general transition from a plane bed with no motion to alternating bars with sediment transport to an upper plane bed (with sheetflow at $S=20\%$ and 30%) as a function of increasing Shields stress. At $S=10\%$, the bed remained stable at Shields stresses much higher than predicted, and once fluvial transport occurred, it only occurred in a very narrow region of Shields stresses before transitioning to upper plane bed conditions around a Shields stress of ~0.2. A similar trend was observed at $S=20\%$, though the transition to upper plane bed conditions developed at average Shields stresses of >0.45, which was close to the transition to mass failure predicted using the model of Takahashi (1978) (at a Shields stress of 0.42). The development of a debris flow or mass failure of the bed was not observed, however. Similarly, at $S = 30\%$, upper plane bed conditions developed close to the predicted transition to mass failure. These data suggest that the Takahashi model for $S < S_c$, under steady uniform flow conditions, does not predict the onset of mass failure. The Takahashi model hypothesizes that debris flows occur due to dispersive pressures generated from grain-grain contacts that lead to mixing throughout the flow depth, suggesting that dispersive pressures capable of supporting the grains in our experiments did not

develop, possibly due to dilatancy or viscous dampening of collisional stresses (Bagnold, 1954; Iverson, 1997; Legros, 2002), or that another particle support mechanism is required (e.g., hindered settling or increased buoyancy from fine-grained sediment).

However, the predicted transition to mass failure did align with the onset of sheetflow for S=20% and S=30%. Sheetflows are concentrated granular slurries that are a hybrid between traditional bedload transport and mass flows (Nnadi and Wilson, 1992; Asano, 1993; Pugh and Wilson, 1999). In the granular mechanics literature, sheetflows may be similar to stage 3 transport, where several grain layers beneath the surface may be mobilized by downward momentum transfer from moving grains and fluid above (Frey and Church, 2011). Sheetflows commonly occur on lower gradient sandy beds under high bed stresses (Nnadi and Wilson, 1992; Pugh and Wilson, 1999), sometimes moving in low amplitude wave-like features called "bedload sheets" (Venditti et al., 2008; Recking et al., 2009), but have not been well documented in steep streams. We found that sheetflow thickness increased with steeper bed slopes, unlike sheetflows at lower bed gradients, and particle velocities increased with bed shear velocity, similar to sheetflows on lower bed gradients (Palucis et al., 2018). This is in contrast to discrete element modeling by Ferdowsi et al. (2017), who found that creep motion in granular beds is independent of shear rate for Shields stresses up to five times the critical Shields stress, though they used bimodal sediment sizes and a horizontal flume bed slope. Understanding the conditions under which these highly-concentrated sheetflow layers occur is important, as they might be considered analogous to the body of a debris flow or occur where hyper-concentrated flood flows or debris floods have been observed (Wells, 1984; Sohn et al., 1999; Hungr et al., 2014), such as on alluvial fans (Stock, 2013).

4.2. Bedform formation on steep slopes

Alternating bar morphology in natural channels generally occurs at $S < 3\%$ (Montgomery and Buffington, 1997; Palucis and Lamb, 2017), and numerous classifications of channel morphology have been proposed in the literature based on field observations on the correspondence of certain channel forms with distinct ranges in bed slope (Rosgen, 1994, 1996; Montgomery and Buffington, 1997; Wohl and Merritt, 2005, 2008; Altunkaynak and Strom, 2009; Buffington and Montgomery, 2013). Despite these field observations, downstream-migrating alternate bars have been produced in the laboratory with bed slopes that exceed $S = 3\%$ (Bathurst et al., 1984; Lisle et al., 1991; Weichert et al., 2008), suggesting that bed slope is not the controlling variable in their formation (Palucis and Lamb, 2017). Recognizing that channel type cannot simply be correlated with bed slope is important for predicting flow and sediment transport conditions in artificial streams or flumes, channels affected by disturbance (i.e., post-fire stream networks), or on other planetary surfaces.

Theoretical work has suggested that channel width-to-depth ratios strongly influence bar formation on lower gradient streams, where alternating bars occur for ratios larger than 12 (Colombini et al., 1987; Parker, 2004). In our experiments, alternate bars tended to form at width-to-depth ratios between 6 and 11, and larger width-to-depth ratios were often associated with planar bed conditions (also see Table S1). This can be problematic when designing experiments or artificial channels to have a specific morphology, as other processes or factors could ultimately control when alternate bars versus plane beds emerge.

The bars we observed at $S = 10\%$ and 20% were morphologically similar to alternate bars in lower gradient streams (Montgomery and Buffington, 1997). Bar wavelength to the channel width ratios were similar to values observed in natural gravel-bedded rivers, where bars are typically spaced every five to seven channel widths apart (Leopold and Wolman, 1957; Knighton,

28

2014), and to width-wavelength relationships observed in lower gradient flume studies (Ikeda, 1984). And like typical gravel bars, the bars that developed in our experiments were elongate features with relatively sharp fronts and a deep pool at the downstream end. At S=20%, the bar aspect ratio (bar height over the wavelength between bars, H_b/λ) decreased with increasing Shields stress, which also has been observed for bars in low gradient flume studies with fine sand to fine gravel beds (Lanzoni, 2000) (Fig. 7a).

The formation mechanisms of bars at S=10% and 20% was different, however, from that described for lower gradient bars. Flume and field studies have shown that bar and pool topography at lower slopes is usually generated by laterally oscillating flow that forces regions of flow convergence, where pools are scoured, and regions of flow divergence, where sediment is deposited to form bars (Dietrich and Smith, 1983; Dietrich and Whiting, 1989; Nelson et al., 2010). The alternating bars observed in our steep experiments were distinctive in that the flow did not deposit sediment on the bar tops in regions of flow divergence. Also, bars at $S = 10\%$ 'stepped' down the flume (Fig. 3b), suggesting a hybrid channel morphology between alternate bars and step pools (Palucis and Lamb, 2017). It is likely that step-pools did not fully develop in our experiments due to width-to-grain diameter ratio ($W_{fl}/D_{84} = 29.5$), which was chosen to suppress the development of granular force chains that might inhibit bed failure, but also suppress the formation of step-pools (Church and Zimmermann, 2007). At S=20%, initial bar formation was mostly erosional (Fig. 4b), which is similar to observations made by Lisle et al. (1991) in flume experiments conducted at S=3% and Lanzoni (2000) at $0.2\% < S < 0.5\%$ (though these bars were stationary due to the development of coarse bar heads). Unlike lower-sloped gravel bars that migrate downstream (Leopold, 1982), bars at S=20% were similar to anti-dunes in that they migrated upstream. The formation of anti-dunes is typically tied to near-critical flow

29

conditions (e.g., Fr > 0.7; Parker, 2004), but for 14 out of 18 runs with upstream migrating bars, the Froude number was less than 0.7. Instead, bars in our experiments appeared to migrate as a result of headward erosion of the lee side of the bar caused by grain failures, likely from seepage (Howard and McLane, 1988), and from fluvial entrainment of grains from the side of the bar. The morphodynamical similarity of alternate bars formed in low gradient systems to those in our experiments has implications for using bedform geometry for hydraulic reconstructions, especially in unique environments (e.g., steep, arid landscapes or other planetary surfaces).

4.3. Comparing flow resistance and sediment flux relations to low gradient channels

For all bed slopes investigated, under no motion cases (i.e., planar beds at the lowest relative submergence), flow resistance coefficients deviate significantly from relations developed for lower gradient rivers (i.e., Manning-Stickler), which is similar to findings in previous steep, plane bed experiments (Bathurst et al., 1984; Cao, 1985; Recking et al., 2008; Prancevic and Lamb, 2015; Lamb et al., 2017a). This suggests that even in the absence of bedforms or sediment transport, baseline flow resistance coefficients are higher in steep channels as opposed to lower gradient deeper rivers.

In the absence of bedforms, but in the presence of intense sediment transport, resistance coefficients were dramatically larger than in both lower gradient flume experiments with dilute bedload transport, as well as steep, no-motion plane bed experiments. These observations, combined with flow resistance coefficient decomposition, support the inference that momentum extraction from sediment transport plays an important role in the momentum balance in steep channels (especially at S=30%) under the transition from bedload to sheetflow. With bedforms, flow resistance coefficients were much higher than predicted by Ferguson (2007), suggesting that momentum losses are occurring due to a combination of grain drag, sediment transport, form

drag from bedforms, and possibly more exchange between the surface flow and the slower moving subsurface flow at the bar boundaries.

Sediment transport relations developed for lower gradient streams, like those by Meyer-Peter-Muller (1948), and later modified by Parker (1979), have been found to over-predict sediment fluxes on steep slopes (e.g., Comiti and Mao, 2012). This was also true for some of the S=10% and 20% cases we investigated, but for S=30% sheetflow cases, the Parker (1979) model significantly under-predicted sediment fluxes. The fact that many relations fail at steep slopes has been suggested to be due to immobile grains or channel-forms (Yager et al., 2007); but even after accounting for bedforms (and momentum losses due to sediment transport), these models still over-predict (rather than under-predict) fluxes we observed, especially for $S \leq 20\%$. Lamb et al. (2008) propose that for steep and shallow flows, there is reduced intensity from turbulence, which can lead to both an increase in the critical Shields stress for initial sediment motion with slope, as well as decreases in sediment flux. This argument was recently supported with turbulence measurements by Lamb et al. (2017a), and could explain why some of the sediment flux data fall below the Parker (1979) model. The Recking et al. (2008) model, which was developed using data from $S \leq 20\%$ and with relative submergence >4, incorporates momentum losses due to intense sediment transport over planar beds. Even though relative submergence was typically <5 in our experiments, and there was likely reduced turbulence intensity (Lamb et al., 2017a), the Recking et al. (2008) model did fairly well, with the exception of sheetflow cases at S=30%. In contrast, the Schneider et al. (2015) model, which accounts for macro-roughness in steep, natural streams with $S \leq 11\%$ and $D > 4$ mm, was a good predictor of fluxes for our experiments with bedforms, but under-predicted fluxes during sheetflow conditions. Lastly, a larger percentage of the total sediment flux was incorporated in the granular sheetflow at 30%, as

31

compared to 20%. At $S = 20\%$, larger τ^* did not result in increases in the sheetflow flux (Fig. 13), hence bedload fluxes must have been increasing. At $S = 30\%$, increases in total flux corresponded to increases in sheetflow flux, suggesting that bedload fluxes were fairly constant and sheetflow fluxes were increasing slightly with τ^*. Thus, while several models were able to adequately predict sediment fluxes for a narrow range of flow or bed state, there was no one sediment transport relation that could predict fluxes for our entire experimental parameter space. This was likely due to lower turbulence intensity and grain drag in our steep, shallow flows, and the development of sheetflow.

5. Conclusions

A series of flume experiments were performed to investigate flow hydraulics, sediment transport rates and intensity, and bedform development on steep bed slopes. With increasing Shields stress at S=10%, we observed the transition from initial motion of sediment on a planar bed, to bedload transport where the bed rapidly developed alternating bars, to a high-energy planar bed. A similar progression occurred at S=20%, however, the development of a planar bed occurred in the presence of concentrated sheetflow. At S=30%, alternate bars did not form, and the transport mode transitioned directly from initial motion to sheetflow. These transport modes and bed states are different compared to low gradient flume studies in several key ways. Initial motion occurred at moderate Shields stresses (0.16 to 0.26) and was accompanied by rapid bed change that was sensitive to small non-uniformities in bed elevation due to transport with grain-scale flow depths. At moderate to high Shields stresses (0.14 to 0.5), alternate bars, similar in scale to those at lower gradients (width-to-wavelength ratios ~ 8), formed at slopes far steeper than typically observed and in some cases migrated upstream under subcritical Froude numbers. Concentrated sheetflows three to ten grain diameters thick developed below the bedload layer at

$\tau^* > 0.3$ for S=20% and 30% and accounted for 15 to 44% of the total sediment flux. Flow resistance coefficients were higher than typical skin friction relations predict, even in experiments with non-moving planar beds, and increased in the presence of bedforms and bedload transport. In general, flow resistance coefficients increased dramatically to $C_f > 1$ as relative submergence decreased to ~ 1, and also with transport stage, with C_f greatest for high energy planar beds due to momentum extraction from sediment transport. Sediment transport models that account for macro-roughness approximately match the bedload fluxes when bedforms were present. However, at high transport stages, these models under-predict the total sediment flux and the contribution due to sheetflows.

Acknowledgements

References

Abbott, J., Francis, J.R.D., 1977. Saltation and suspension trajectories of solid grains in a water stream. Philos. Trans. R. Soc. Lond. Math. Phys. Eng. Sci. 284, 225–254.

Aberle, J., Smart, G.M., 2003. The influence of roughness structure on flow resistance on steep slopes. J. Hydraul. Res. 41, 259–269. https://doi.org/10.1080/00221680309499971

Altunkaynak, A., Strom, K.B., 2009. A predictive model for reach morphology classification in mountain streams using multilayer perceptron methods. Water Resour. Res. 45, W12501. https://doi.org/10.1029/2009WR008055

Asano, T., 1993. Observations of granular-fluid mixture under an oscillatory sheet flow. In: Coastal Engineering 1992. pp. 1895–1909.

Bagnold, R.A., 1954. Experiments on a gravity-free dispersion of large solid spheres in a Newtonian fluid under shear. In: Proceedings of the Royal Society of London A: Mathematical, Physical and Engineering Sciences. The Royal Society, pp. 49–63.

Bathurst, J., Cao, H., Graf, W., 1984. Hydraulics and sediment transport in a steep flume: Data from the EPFL study. Rep. Cent. Ecol. Hydrol. Wallingford UK.

Bathurst, J.C., 1985. Flow resistance estimation in mountain rivers. J. Hydraul. Eng. 111, 625–643.

Berger, C., McArdell, B.W., Schlunegger, F., 2011. Sediment transfer patterns at the Illgraben catchment, Switzerland: implications for the time scales of debris flow activities. Geomorphology 125, 421–432.

Bridge, J.S., 1981. A discussion of Bagnold's (1956) bedload transport theory in relation to recent developments in bedload modelling. Earth Surf. Process. Landf. 6, 187–190.

Buffington, J.M., Montgomery, D.R., 2013. Geomorphic classification of rivers. pp. 730–767.

Buffington, J.M., Montgomery, D.R., Greenberg, H.M., 2004. Basin-scale availability of salmonid spawning gravel as influenced by channel type and hydraulic roughness in mountain catchments. Can. J. Fish. Aquat. Sci. 61, 2085–2096.

Cannon, S.H., Gartner, J.E., Wilson, R.C., Bowers, J.C., Laber, J.L., 2008. Storm rainfall conditions for floods and debris flows from recently burned areas in southwestern Colorado and southern California. Geomorphology 96, 250–269.

Cao, H.H., 1985. Résistance hydraulique d" un lit de gravier mobile à pente raide.

Chiew, Y.-M., Parker, G., 1994. Incipient sediment motion on non-horizontal slopes. J. Hydraul. Res. 32, 649–660.

Chin, A., Wohl, E., 2005. Toward a theory for step pools in stream channels. Prog. Phys. Geogr. 29, 275–296.

Church, M., 2002. Geomorphic thresholds in riverine landscapes. Freshw. Biol. 47, 541–557. https://doi.org/10.1046/j.1365-2427.2002.00919.x

Church, M., Zimmermann, A., 2007. Form and stability of step-pool channels: Research progress. Water Resour. Res. 43, W03415. https://doi.org/10.1029/2006WR005037

Church, M., Hassan, M.A., Wolcott, J.F., 1998. Stabilizing self-organized structures in gravel-bed stream channels: field and experimental observations. Water Resour. Res. 34, 3169–3179.

Coe, J.A., Kinner, D.A., Godt, J.W., 2008. Initiation conditions for debris flows generated by runoff at Chalk Cliffs, central Colorado. Geomorphology, Debris flows initiated by runoff, erosion, and sediment entrainment in western North America 96, 270–297. https://doi.org/10.1016/j.geomorph.2007.03.017

Colombini, M., Seminara, G., Tubino, M., 1987. Finite-amplitude alternate bars. J. Fluid Mech. 181, 213–232. https://doi.org/10.1017/S0022112087002064

Comiti, F., Mao, L., 2012. Recent advances in the dynamics of steep channels. Gravel-bed rivers: processes, tools, environments. Wiley online library, pp. 351 - 377.

Dietrich, W.E., Smith, J.D., 1983. Influence of the point bar on flow through curved channels. Water Resour. Res. 19, 1173–1192. https://doi.org/10.1029/WR019i005p01173

Dietrich, W.E., Whiting, P., 1989. Boundary shear stress and sediment transport in river meanders of sand and gravel. In: Ikeda, S., Parker, G. (Eds.), River Meandering. American Geophysical Union, pp. 1–50.

Einstein, H., Banks, R., 1950. Fluid resistance of composite roughness. Eos Trans. Am. Geophys. Union 31, 603–610.

Farnebäck, G., 2003. Two-frame motion estimation based on polynomial expansion, in: Scandinavian Conference on Image Analysis. Springer, pp. 363–370.

Ferdowsi, B., Ortiz, C.P., Houssais, M., Jerolmack, D.J., 2017. River-bed armouring as a granular segregation phenomenon. Nat. Commun. 8, 1363.

Ferguson, R., 2007. Flow resistance equations for gravel- and boulder-bed streams. Water Resour. Res. 43, W05427. https://doi.org/10.1029/2006WR005422

Ferguson, R.I., 2012. River channel slope, flow resistance, and gravel entrainment thresholds. Water Resour. Res. 48.

Fernandez Luque, R., Van Beek, R., 1976. Erosion and transport of bed-load sediment. J. Hydraul. Res. 14, 127–144.

Folk, R.L., Ward, W.C., 1957. Brazos River bar [Texas]; a study in the significance of grain size parameters. J. Sediment. Res. 27, 3–26.

Frey, P., Church, M., 2011. Bedload: a granular phenomenon. Earth Surf. Process. Landf. 36, 58–69.

Gao, P., 2008. Transition between two bed-load transport regimes: saltation and sheet flow. J. Hydraul. Eng., 134, 340-349.

Graf, W., Cao, H., Suszka, L., 1987. Hydraulics of steep, mobile-bed channels. EV.

Grant, G.E., Swanson, F.J., Wolman, M.G., 1990. Pattern and origin of stepped-bed morphology in high-gradient streams, Western Cascades, Oregon. Geol. Soc. Am. Bull. 102, 340–352. https://doi.org/10.1130/0016-7606(1990)102<0340:PAOOSB>2.3.CO;2

Hassan, M.A., Reid, I., 1990. The influence of microform bed roughness elements on flow and sediment transport in gravel bed rivers. Earth Surf. Process. Landf. 15, 739–750. https://doi.org/10.1002/esp.3290150807

Hongve, D., 1987. A revised procedure for discharge measurement by means of the salt dilution method. Hydrol. Process. 1, 267–270.

Howard, A.D., McLane, C.F., 1988. Erosion of cohesionless sediment by groundwater seepage. Water Resour. Res. 24, 1659–1674. https://doi.org/10.1029/WR024i010p01659

Hungr, O., Leroueil, S., Picarelli, L., 2014. The Varnes classification of landslide types, an update. Landslides 11, 167–194.

Ikeda, S., 1984. Prediction of alternate bar wavelength and height. J. Hydraul. Eng. 110, 371–386.

Iseya, F., Ikeda, H., 1987. Pulsations in bedload transport rates induced by a longitudinal sediment sorting: a flume study using sand and gravel mixtures. Geogr. Ann. Ser. Phys. Geogr. 69, 15–27.

Iverson, R.M., 1997. The physics of debris flows. Rev. Geophys. 35, 245–296. https://doi.org/10.1029/97RG00426

Jakob, M., Hungr, O., Jakob, D.M., 2005. Debris-flow hazards and related phenomena. Springer.

Johnston, C.E., Andrews, E., Pitlick, J., 1998. In situ determination of particle friction angles of fluvial gravels. Water Resour. Res. 34, 2017–2030.

Jop, P., Forterre, Y., Pouliquen, O., 2005. Crucial role of sidewalls in granular surface flows: consequences for the rheology. J. Fluid Mech. 541, 167–192.

Knighton, D., 2014. Fluvial Forms and Processes: A New Perspective. Routledge.

Lamb, M.P., Dietrich, W.E., Venditti, J.G., 2008. Is the critical Shields stress for incipient sediment motion dependent on channel-bed slope? J. Geophys. Res. Earth Surf. 113, F02008. https://doi.org/10.1029/2007JF000831

Lamb, M.P., Levina, M., DiBiase, R.A., Fuller, B.M., 2013. Sediment storage by vegetation in steep bedrock landscapes: Theory, experiments, and implications for postfire sediment yield. J. Geophys. Res. Earth Surf. 118, 1147–1160.

Lamb, M.P., Finnegan, N.J., Scheingross, J.S., Sklar, L.S., 2015. New insights into the mechanics of fluvial bedrock erosion through flume experiments and theory. Geomorphology 244, 33–55.

Lamb, M.P., Brun, F., Fuller, B.M., 2017a. Hydrodynamics of steep streams with planar coarse-grained beds: turbulence, flow resistance, and implications for sediment transport. Water Resour. Res.

Lamb, M.P., Brun, F., Fuller, B.M., 2017b. Direct measurements of lift and drag on shallowly submerged cobbles in steep streams: Implications for flow resistance and sediment transport. Water Resour. Res.

Lanzoni, S., 2000. Experiments on bar formation in a straight flume: 2. Graded sediment. Water Resour. Res. 36, 3351–3363.

Legros, F., 2002. Can dispersive pressure cause inverse grading in grain flows? J. Sediment. Res. 72, 166–170.

Leopold, L., 1982. Water surface topography in river channels and implications for meander development. Wiley, Chichester.

Leopold, L.B., Wolman, M.G., 1957. River channel patterns: braided, meandering, and straight. US Government Printing Office.

Lisle, T.E., Ikeda, H., Iseya, F., 1991. Formation of stationary alternate bars in a steep channel with mixed-size sediment: a flume experiment. Earth Surf. Process. Landf. 16, 463–469. https://doi.org/10.1002/esp.3290160507

McCoy, S., Kean, J., Coe, J., Tucker, G., Staley, D., Wasklewicz, T., 2012. Sediment entrainment by debris flows: in situ measurements from the headwaters of a steep catchment. J. Geophys. Res. Earth Surf. 117.

Meyer-Peter, E., Müller, R., 1948. Formulas for Bed-Load transport. IAHSR 2nd Meet. Stockh. Append. 2.

Miller, M., McCave, I., Komar, P., 1977. Threshold of sediment motion under unidirectional currents. Sedimentology 24, 507–527.

Miller, R.L., Byrne, R.J., 1966. The angle of repose for a single grain on a fixed rough bed. Sedimentology 6, 303–314.

Milliman, J.D., Syvitski, J.P.M., 1992. Geomorphic/tectonic control of sediment discharge to the ocean: the importance of small mountainous rivers. J. Geol. 100, 525–544.

Mizuyama, T., 1977. Bedload transport in steep channels.

Montgomery, D.R., Buffington, J.M., 1997. Channel-reach morphology in mountain drainage basins. Geol. Soc. Am. Bull. 109, 596–611. https://doi.org/10.1130/0016-7606(1997)109<0596:CRMIMD>2.3.CO;2

Montgomery, D.R., Massong, T.M., Hawley, S.C.S., 2003. Influence of debris flows and log jams on the location of pools and alluvial channel reaches, Oregon Coast Range. Geol. Soc. Am. Bull. 115, 78–88. https://doi.org/10.1130/0016-7606(2003)115<0078:IODFAL>2.0.CO;2

Mueller, E., Batalla, R., Garcia, C., Bronstert, A., 2008. Modeling bed-load rates from fine grain-size patches during small floods in a gravel-bed river. J. Hydraul. Eng. 134, 1430–1439.

Nelson, P.A., Dietrich, W.E., Venditti, J.G., 2010. Bed topography and the development of forced bed surface patches. J. Geophys. Res. 115. https://doi.org/10.1029/2010JF001747

Nitsche, M., Rickenmann, D., Turowski, J.M., Badoux, A., Kirchner, J.W., 2011. Evaluation of bedload transport predictions using flow resistance equations to account for macro-roughness in steep mountain streams. Water Resour. Res. 47, W08513. https://doi.org/10.1029/2011WR010645

Nnadi, F.N., Wilson, K.C., 1992. Motion of contact-load particles at high shear stress. J. Hydraul. Eng. 118, 1670–1684.

Palucis, M., Lamb, M., 2017. What controls channel form in steep mountain streams? Geophys. Res. Lett.

Palucis, M.C., Ulizio, T., Fuller, B., Lamb, M.P., 2018. Intense granular sheetflow in steep streams. Geophys. Res. Lett.

Parker, G., 2004. 1D Sediment transport morphodynamics with applications to rivers and turbidity currents, E-book. St. Anthony Falls Lab Univ Minn Minneap. Httphydrolab Ill. Edupeopleparkergmorphodynamicse-Book Htm.

Parker, G., 1979. Hydraulic geometry of active gravel rivers. J. Hydraul. Div. 105, 1185–1201.

Prancevic, J.P., Lamb, M.P., 2015. Particle friction angles in steep mountain channels. J. Geophys. Res. Earth Surf. 120, 242–259.

Prancevic, J.P., Lamb, M.P., Fuller, B.M., 2014. Incipient sediment motion across the river to debris-flow transition. Geology 42, 191–194. https://doi.org/10.1130/G34927.1

Prancevic, J.P., Lamb, M.P., Palucis, M.C., Venditti, J.G., 2018. The role of three-dimensional boundary stresses in limiting the occurrence and size of experimental landslides. J. Geophys. Res. Earth Surf. 123, 46–65.

Pugh, F.J., Wilson, K.C., 1999. Velocity and concentration distributions in sheet flow above plane beds. J. Hydraul. Eng. 125, 117–125.

Recking, A., 2006. An experimental study of grain sorting effects on bedload. Grenoble University.

Recking, A., 2010. A comparison between flume and field bed load transport data and consequences for surface-based bed load transport prediction. Water Resour. Res. 46.

Recking, A., Frey, P., Paquier, A., Belleudy, P., Champagne, J.-Y., 2008. Feedback between bed load transport and flow resistance in gravel and cobble bed rivers. Water Resour. Res. 44.

Recking, A., Bacchi, V., Naaim, M., Frey, P., 2009. Antidunes on steep slopes. J. Geophys. Res. Earth Surf. 114, F04025. https://doi.org/10.1029/2008JF001216

Rickenmann, D., 1990. Bedload transport capacity of slurry flows at steep slopes. Mitteilungen Vers. Wasserbau Hydrol. Glaziologie Eidgenossischen Tech. Hochsch. Zurich.

Rickenmann, D., 1997. Sediment transport in Swiss torrents. Earth Surf. Process. Landf. 22, 937–951.

Rickenmann, D., Recking, A., 2011. Evaluation of flow resistance in gravel-bed rivers through a large field data set. Water Resour. Res. 47.

Rosgen, D.L., 1994. A classification of natural rivers. Catena 22, 169–199.

Rosgen, D.L., 1996. Applied river morphology. Wildland Hydrology.

Scheingross, J.S., Winchell, E.W., Lamb, M.P., Dietrich, W.E., 2013. Influence of bed patchiness, slope, grain hiding, and form drag on gravel mobilization in very steep streams. J. Geophys. Res. Earth Surf. 118, 982–1001.

Schneider, J.M., Rickenmann, D., Turowski, J.M., Bunte, K., Kirchner, J.W., 2015. Applicability of bed load transport models for mixed-size sediments in steep streams considering macro-roughness. Water Resour. Res. 51, 5260–5283.

Shields, A., 1936. Application of similarity principles and turbulence research to bed-load movement.

Shreve, R.L., 1969. Stream Lengths and Basin Areas in Topologically Random Channel Networks. J. Geol. 77, 397–414.

Smart, G.M., Jäggi, M., 1983. Sedimenttransport in steilen Gerinnen: Sediment transport on steep slopes. Versuchsanst. für Wasserbau, Hydrologie u. Glaziologie an d. Eidgenöss. Techn. Hochsch.

Sohn, Y.K., Rhee, C.W., Kim, B.C., 1999. Debris flow and hyperconcentrated flood-flow deposits in an alluvial fan, northwestern part of the Cretaceous Yongdong Basin, Central Korea. J. Geol. 107, 111–132.

Stock, J., 2013. 9.23 Waters Divided: A History of Alluvial Fan Research and a View of Its Future.

Stock, J., Dietrich, W.E., 2003. Valley incision by debris flows: Evidence of a topographic signature. Water Resour. Res. 39, 1089. https://doi.org/10.1029/2001WR001057

Takahashi, T., 1978. Mechanical characteristics of debris flow. J. Hydraul. Div. 104, 1153–1169.

Takahashi, T., 2007. Debris flow mechanics, prediction and countermeasurements. Taylor and Francis Group.

Trampush, S.M., Huzurbazar, S., McElroy, B., 2014. Empirical assessment of theory for bankfull characteristics of alluvial channels. Water Resour. Res. 50, 9211–9220. https://doi.org/10.1002/2014WR015597

Turowski, J.M., Yager, E.M., Badoux, A., Rickenmann, D., Molnar, P., 2009. The impact of exceptional events on erosion, bedload transport and channel stability in a step-pool channel. Earth Surf. Process. Landf. 34, 1661–1673.

Vanoni, V.A., Brooks, N.H., 1957. Laboratory studies of the roughness and suspended load of alluvial streams.

Venditti, J., Nelson, P., Dietrich, W., 2008. The domain of bedload sheets. Mar. River Dune Dyn. Leeds U. K.

Weichert, R.B., Bezzola, G.R., Minor, H.-E., 2008. Bed morphology and generation of step–pool channels. Earth Surf. Process. Landf. 33, 1678–1692.

Wells, N.A., 1984. Sheet debris flow and sheetflood conglomerates in Cretaceous cool-maritime alluvial fans, South Orkney Islands, Antarctica.

Wilcox, A.C., Nelson, J.M., Wohl, E.E., 2006. Flow resistance dynamics in step-pool channels: 2. Partitioning between grain, spill, and woody debris resistance. Water Resour. Res. 42.

Wilcock, P., Pitlick, J., Cui, Y., 2009. Sediment transport primer: estimating bed-material transport in gravel-bed rivers.

Wohl, E., Merritt, D., 2005. Prediction of mountain stream morphology. Water Resour. Res. 41, W08419. https://doi.org/10.1029/2004WR003779

Wohl, E., Merritt, D.M., 2008. Reach-scale channel geometry of mountain streams. Geomorphology 93, 168–185. https://doi.org/10.1016/j.geomorph.2007.02.014

Yager, E.M., Kirchner, J.W., Dietrich, W.E., 2007. Calculating bed load transport in steep boulder bed channels. Water Resour. Res. 43, W07418. https://doi.org/10.1029/2006WR005432

Yager, E.M., Turowski, J.M., Rickenmann, D., McArdell, B.W., 2012. Sediment supply, grain protrusion, and bedload transport in mountain streams. Geophys. Res. Lett. 39, L10402. https://doi.org/10.1029/2012GL051654

Zimmermann, A., Church, M., Hassan, M.A., 2010. Step-pool stability: Testing the jammed state hypothesis. J. Geophys. Res. Earth Surf. 115, F02008. https://doi.org/10.1029/2009JF001365

Notation

The following symbols are used in this paper:

A = area

C = constant that depends on the velocity profile shape near the bed surface

C_b = solid fraction (by volume) of sheetflow layer

$C_{b,bed}$ = solid fraction (by volume) in the static bed

$C_{D,sub}$ = median drag coefficient for submerged particles

C_f = total flow resistance coefficient

$C_{f,bedforms}$ = flow resistance coefficient due to morphologic drag

$C_{f,bedload}$ = flow resistance coefficient due to sediment bedload transport

$C_{f,grain}$ = flow resistance coefficient due to grain drag

$C_{L,sub}$ = median lift coefficient for submerged particles

D = grain diameter

D_{50} = median grain diameter

D_{84} = grain diameter for which 84% of the grains are smaller

D_o = reference grain diameter, 1 mm

F_L/F_D = lift to drag coefficient ratio

Fr = Froude number

f_w = fraction of the channel banks that were smooth

g = acceleration due to gravity

H = clear water flow depth

H_b = bar height

39

H_{bed} = thickness of the sediment bed

H_g = granular sheetflow thickness

k_s = bed roughness height

n_p = number of grains

Q = total discharge

q_s = total volumetric transport rate per unit width

Q_{sub} = sub-surface discharge

Q_{sur} = surface discharge

R = submerged density of quartz

Re_p = Reynold's particle number

R_h = hydraulic radius

S = bed slope = $\tan\theta$

S_c = critical slope

U = depth-averaged water flow velocity

$u*$ = bed shear velocity

u_o = seepage velocity at the bed surface

U_p = mean particle velocity

U_{sub} = mean subsurface velocity

V_p = volume of a grain, assuming it is a sphere

W = channel width

W_{fl} = flume width

z = bed elevation relative to flume bottom

Φ = Einstein number, non-dimensional sediment flux

ϕ = phi value

ϕ_d = dry angle of repose

ϕ_o = pocket friction angle

ϕ_{ps} = partially saturated angle of repose

η = porosity of gravel

λ = bar wavelength

ν = kinematic viscosity of water

θ = bed slope angle

ρ_s = density of sediment

ρ = density of water

σ = sorting coefficient

τ^* = Shields stress, non-dimensional

τ_b = bed stress, dimensional

$\tau_{b,grain}$ = bed stress due to grain resistance alone, dimensional

τ_c^* = critical Shields stress for initial sediment motion, non-dimensional

τ_g^* = grain Shields stress, non-dimensional

τ_m = shear stress spent on morphologic drag, dimensional

τ_r^* = reference Shields stress, non-dimensional

τ_T = total stress on the bed, dimensional

Figures and Captions
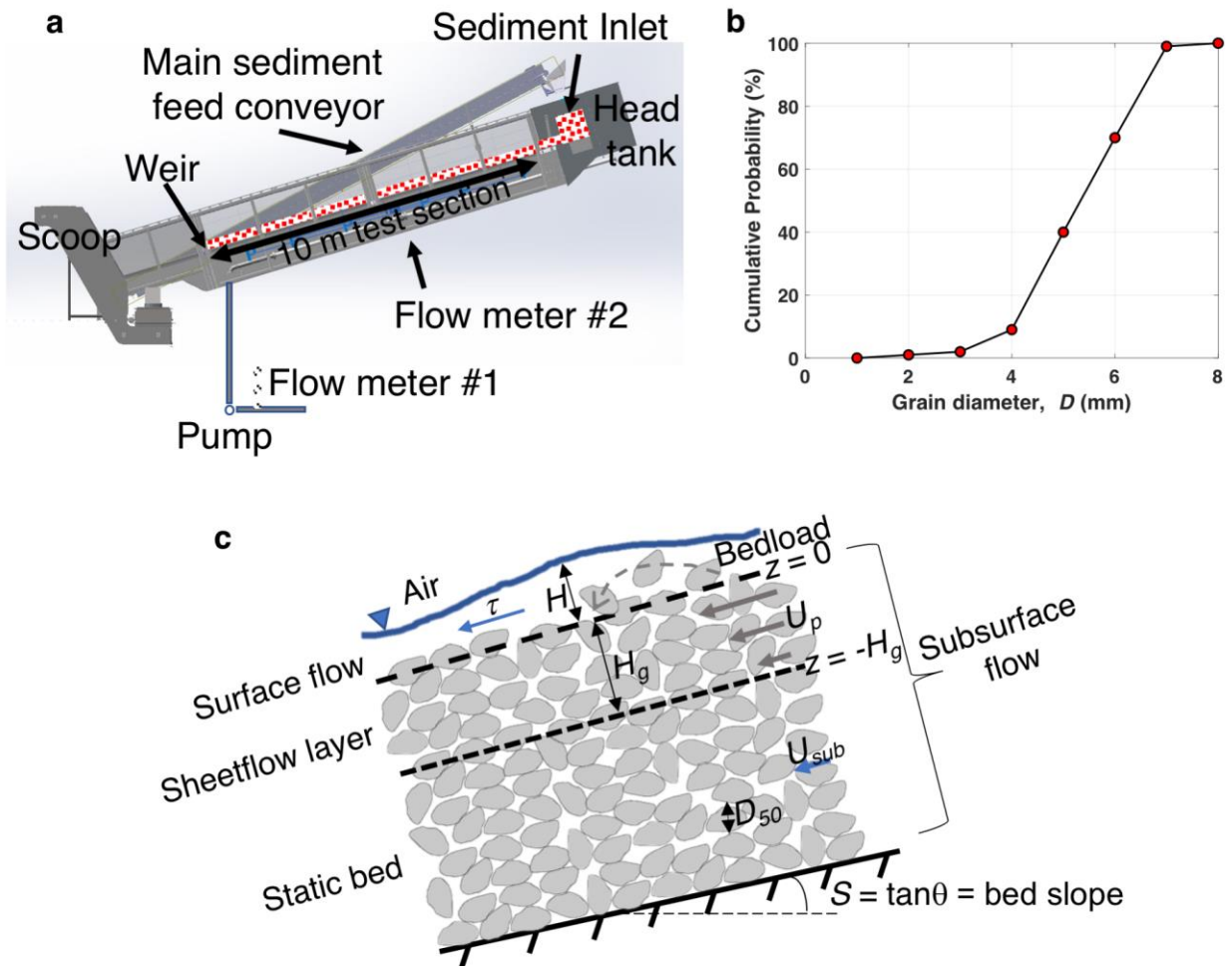
Figure 1. (a) Cartoon schematic of the main test section of the tilting flume located at the California Institute of Technology (not shown are the end tank, the sediment hoppers, and the secondary sediment conveyors). Sediment fed from the hoppers and/or secondary conveyors is transported into the flume via the main sediment feed conveyor, whereas water is introduced via the head tank. Sediment exiting the test section is collected after the weir for sediment flux measurements. Weir height and porosity are adjusted at each slope to maintain steady, uniform water flow conditions. Water exiting the flume is re-circulated through the end tank and pump system, while sediment is re-circulated via the scoop and sediment conveyors. (b) Grain size distribution of the gravel used in the experiments. The median grain size is 5.4 mm and the D_{84} is

6.1 mm, (c) Schematic of zones of flow and sediment transport for the surface ($z>0$) and the subsurface ($z < 0$), with a bed slope of S. The surface flow depth is H with a mean flow velocity U. Particles transported in the surface flow are transported as bedload, such that the base of the surface flow is at the base of the bedload layer. In cases, a dense granular sheetflow layer (thickness H_g) developed within the bed (initial bed thickness is H_{bed}), with a mean particle velocity of U_p. U_{sub} is the mean fluid subsurface flow velocity.
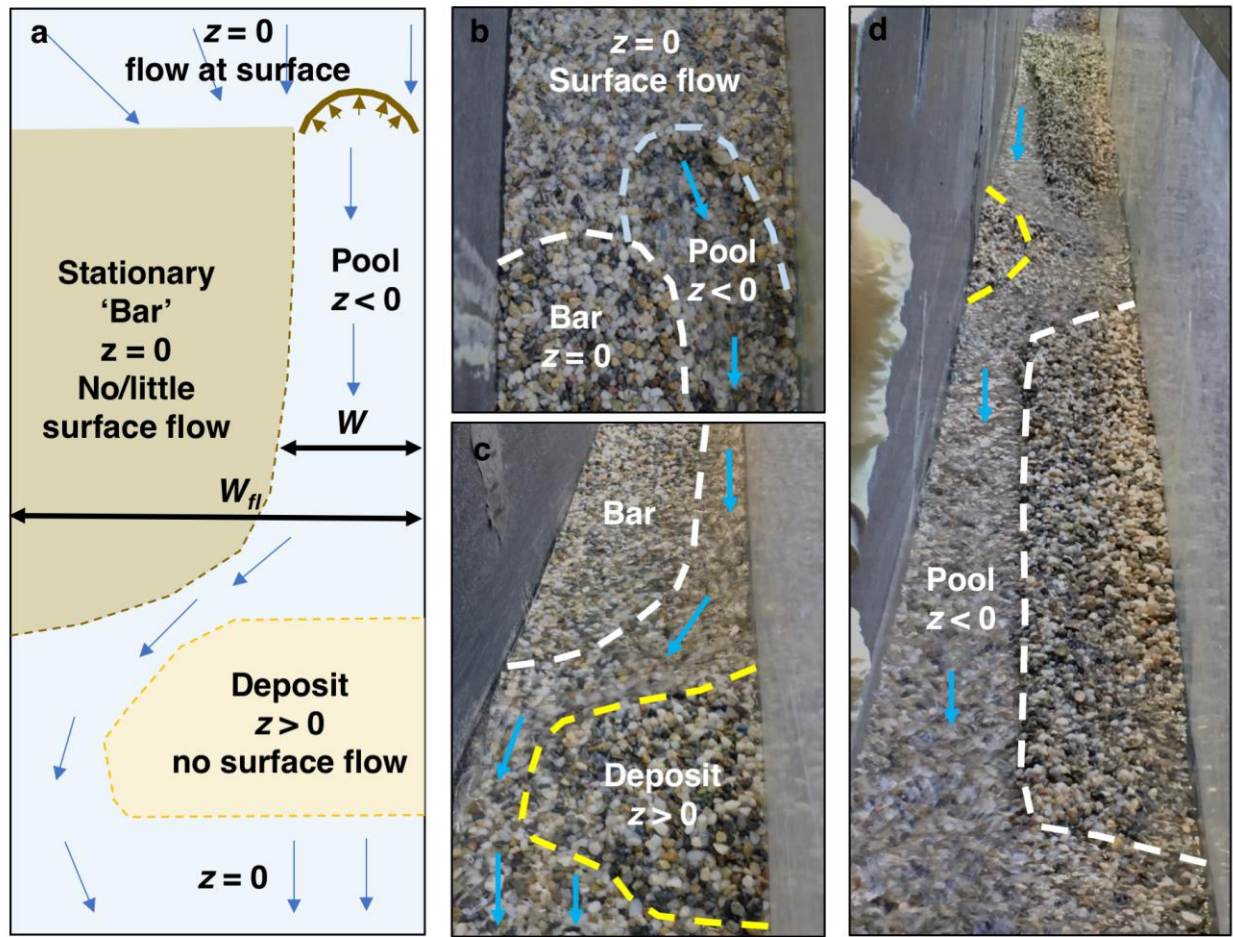
Figure 2. The bed at initial motion conditions at $S=10\%$. (a) a cartoon schematic of the bed showing zone of incision with surface flow (z<0, colored blue), deposition (z>0, colored yellow) and areas where the bed remains unchanged from its initial state with no surface flow ($z=0$,

colored brown), (c) a close up of the deposit building up at the downstream end of the pool, and
(d) a view of the bed looking upstream, showing several bar-pool units. The blue arrows indicate
the direction of surface water flow, the white dashed lines outline bar units, the yellow dashed
lines outline regions deposited by the flow, and the light blue dashed lines outline the heads of
pools. Images (b) and (c) were taken from Experiment 68 (Table S1) with $\tau^* = 0.17$.
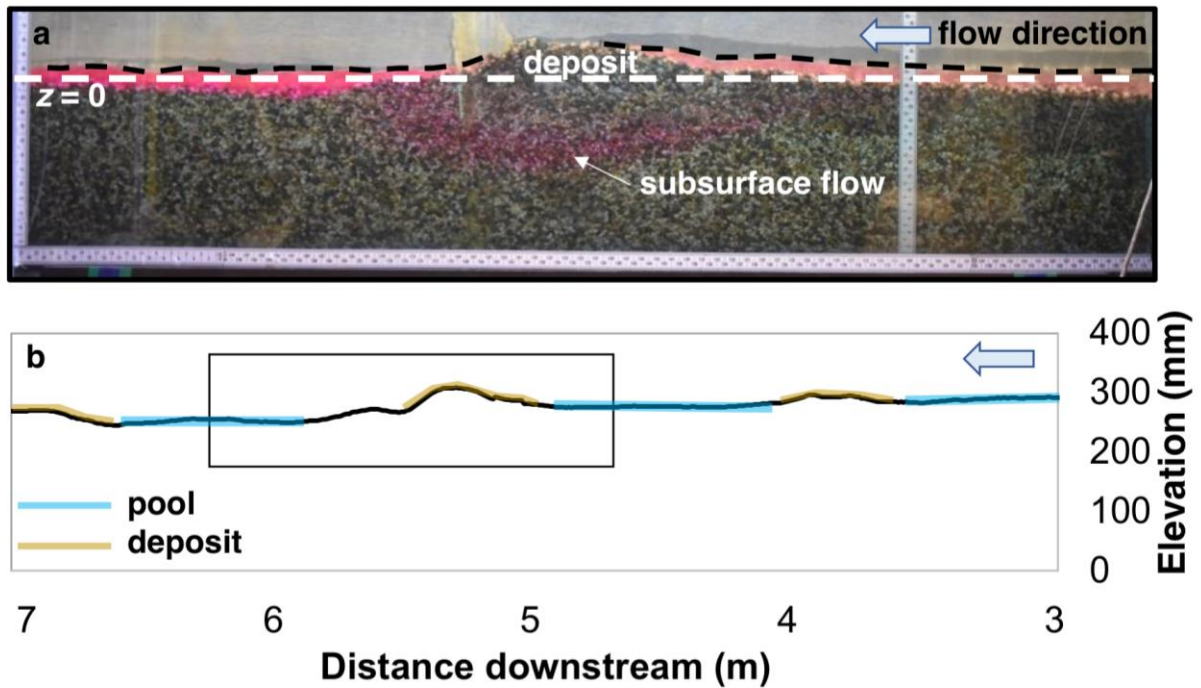
Figure 3. (a) Side-view of the bed at S=10% at initial motion, where the white dashed line shows
the initial elevation of the bed and the black dash line traces the air-water interface, and (b) A
long profile of the bed (pools outlined in blue and deposits outlined in light brown) from 3 m to 7
m in the test section of the flume, with the region shown in (a) boxed in. The blue arrow
indicates the water flow direction. Note the subsurface flow (labeled) as indicated by the pink
dye in (a). Taken from Experiment 68 (Table S1) with $\tau^* = 0.17$.
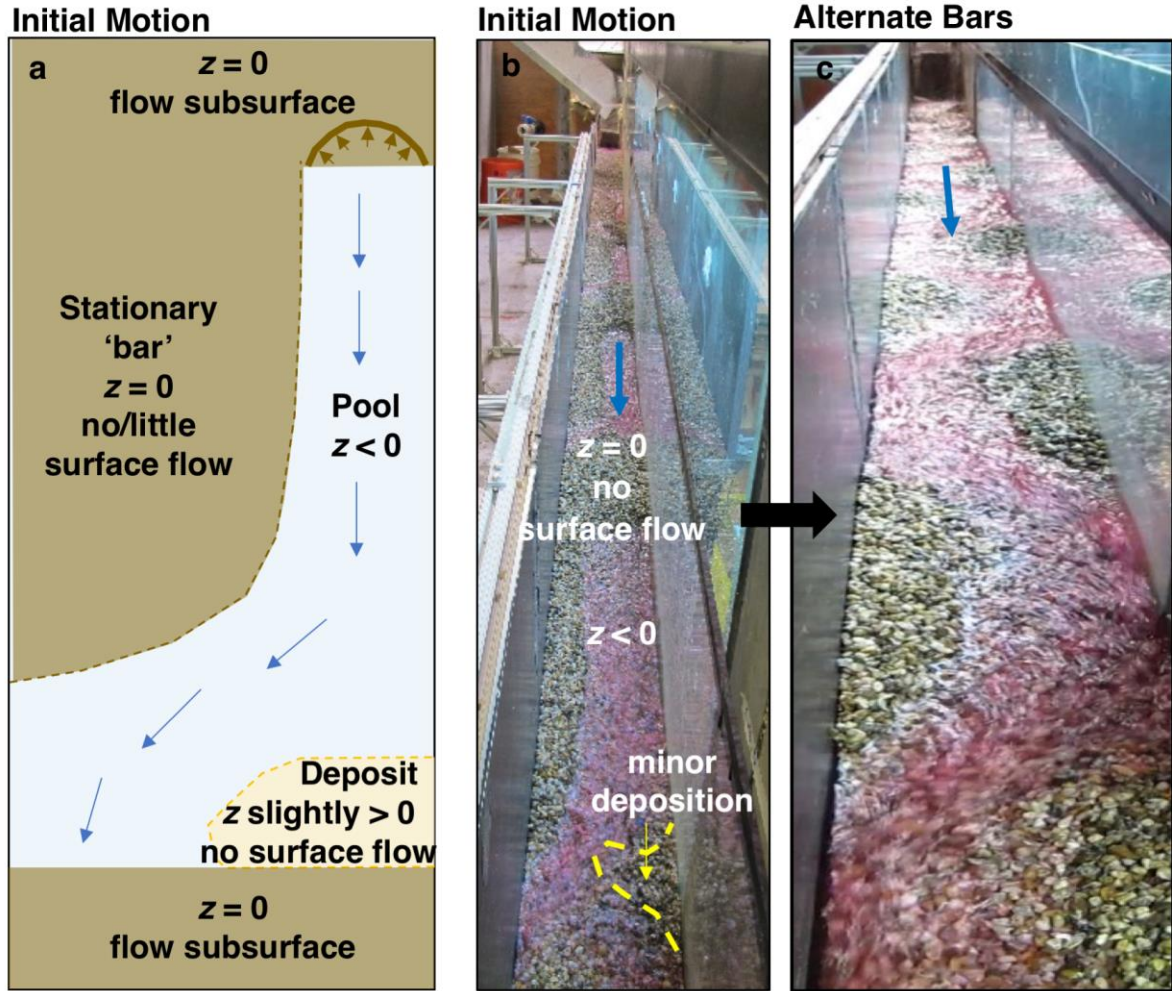
Figure 4. Initial motion conditions and the transition to alternating bars at S=20% for Experiment 27 and 10 (Table S1) at Shields stresses of 0.23 and 0.39, respectively (a) Cartoon schematic of the bed showing zone of incision with surface flow (z<0, colored blue), deposition (z>0, colored yellow) and areas where the bed remains unchanged from its initial state (z=0, colored brown), (b) a view of the bed looking upstream, showing several bed-pool units, and (c) the bed after transitioning to alternate bars. The blue arrows indicate the direction of surface water flow (pink flow in (b) and (c)) and the yellow dashed line indicates regions deposited by the flow.

44
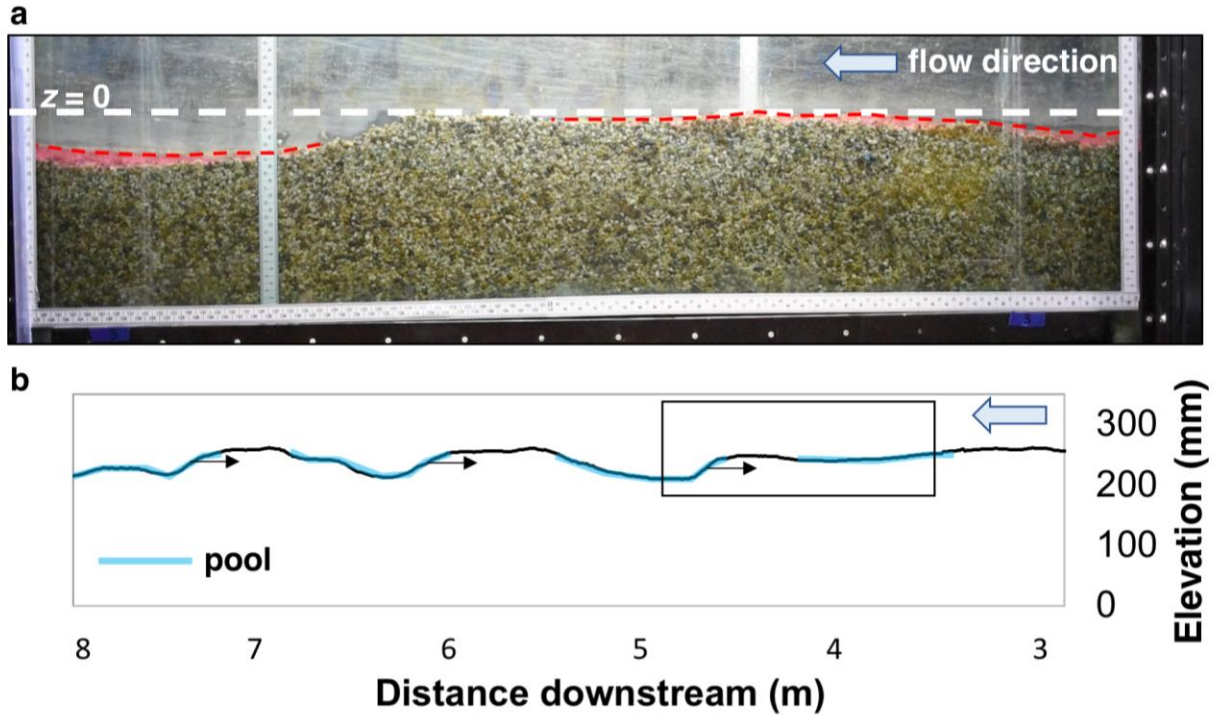
Figure 5. (a) Side-view of the bed at *S*=20% at initial motion for Experiment 27 (Table S1) at a Shields stress of 0.23, where the white dashed line shows the initial elevation of the bed and the black dash line indicates the air-water interface (surface flow dyed pick), and (b) long profile of the bed (pools outlined in blue) from 3 m to 8 m in the test section of the flume, with the region shown in (a) boxed in. The black arrows indicate the direction of migration of the pool-head and the blue arrows indicate the water flow direction.
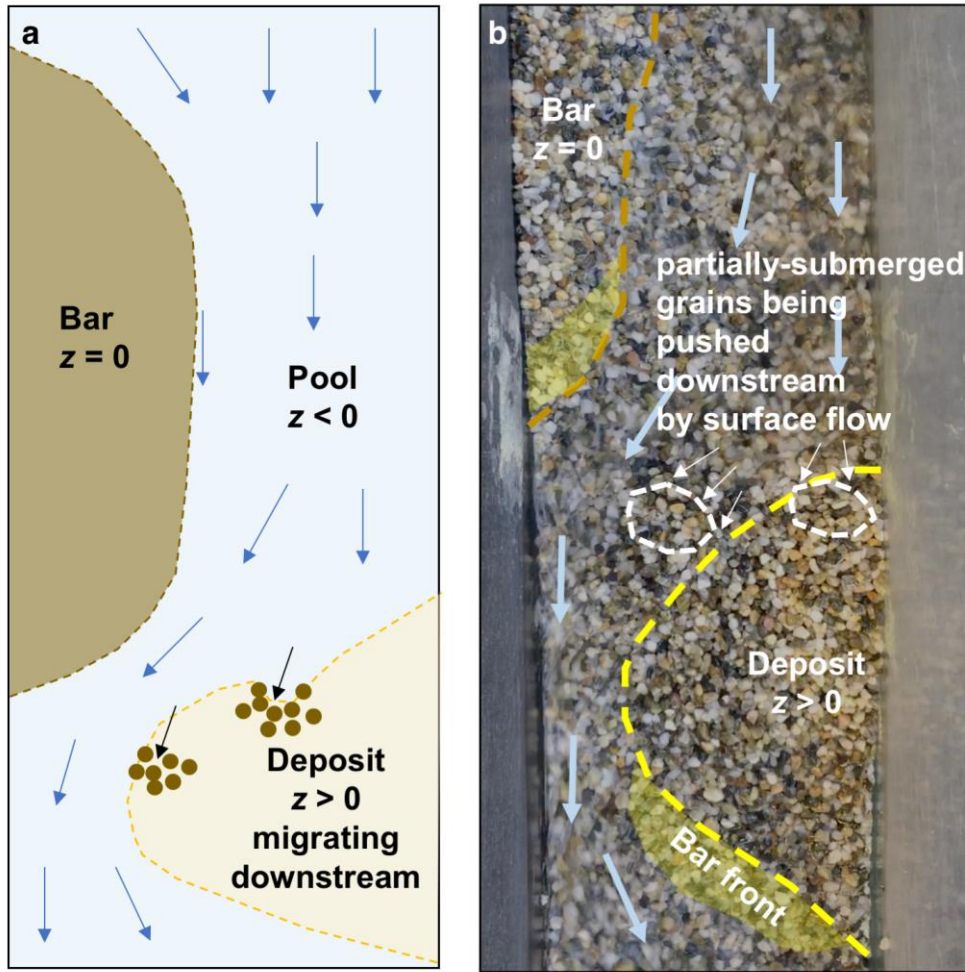
Figure 6. The bed at alternate bar conditions at *S*=10% for Experiment 20 (Table S1) at a Shields stress of 0.19. (a) Cartoon schematic of the bed showing zone of incision (*z*< 0, colored blue), deposition (*z*>0, colored yellow) and areas where the bed remains unchanged from its initial state (*z*=0, colored brown), and (b) a close-up view of the bed looking at the regions where sediment is being mobilized downstream (white dashed lines), regions of deposition (yellow dashed line), and deposition of the bar front (yellow region) which led to downstream migration of the bars/deposits.
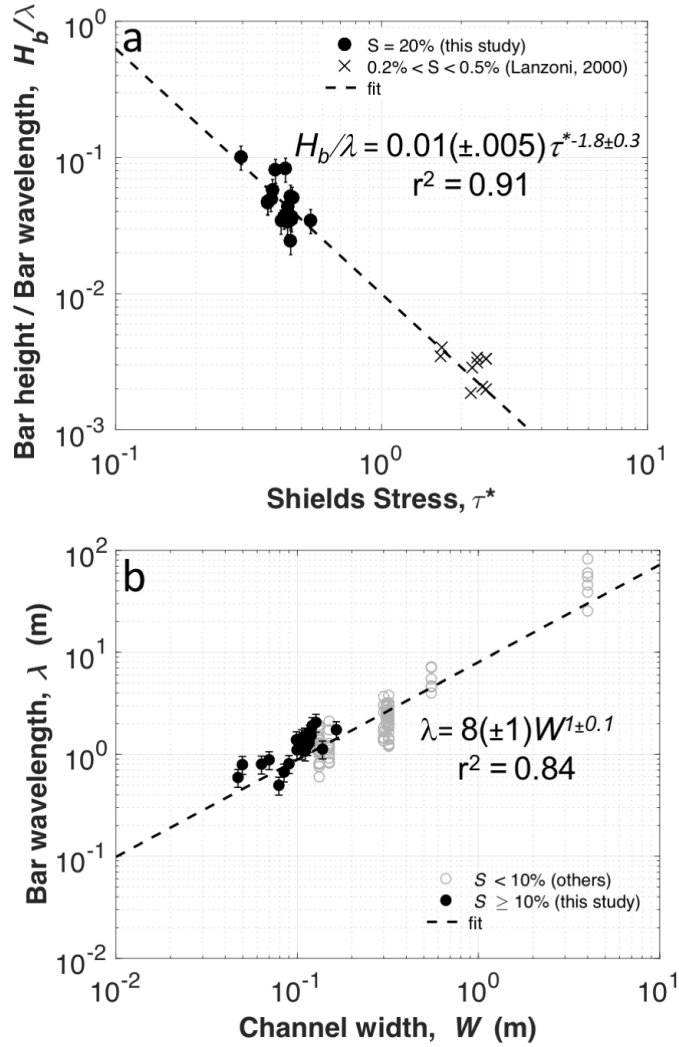
Figure 7. (a) The ratio of bar height to bar wavelength (± relative error) as a function of Shields stress for *S*=20% and compared to low gradient flume data from Lanzoni (2000), and (b) bar wavelength plotted as a function of the channel width (grey circles are from flume data at *S*<10% (Ikeda, 1984) and black circles are the data from these flume experiments).
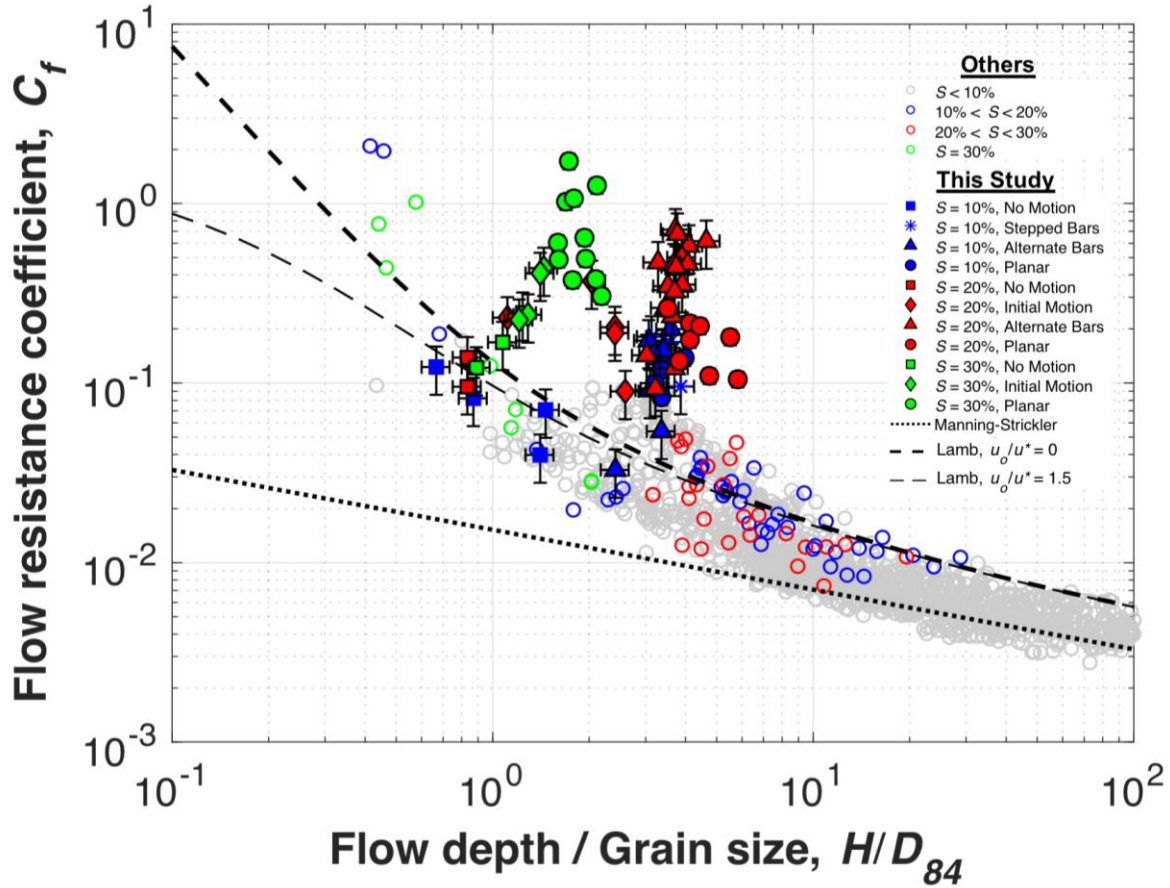
47

Figure 8. Total flow resistance coefficient, C_f, plotted as a function of H/D_{84}. The grey open circles are from previous flume experiments for $S<10\%$ (Bathurst et al., 1984; Ikeda, 1984; Recking, 2006; Lamb et al., 2017a), while the open blue, red, and green circles are from Lamb et al. (2017b) and Bathurst et al. (1984) at S=10%, 20%, and 30% respectively. Data from these experiments are shown with filled blue, red, and green markers for S=10%, 20%, and 30% respectively. Squares are for no motion cases, diamonds are for initial motion cases, triangles are for alternate bar cases, and circles are for planar beds. These data are compared to the Manning-Strickler relation, as well as the Lamb et al. (2017b) model for u_o/u^*=0 and u_o/u^*=1.5. Error bars represent the relative error.
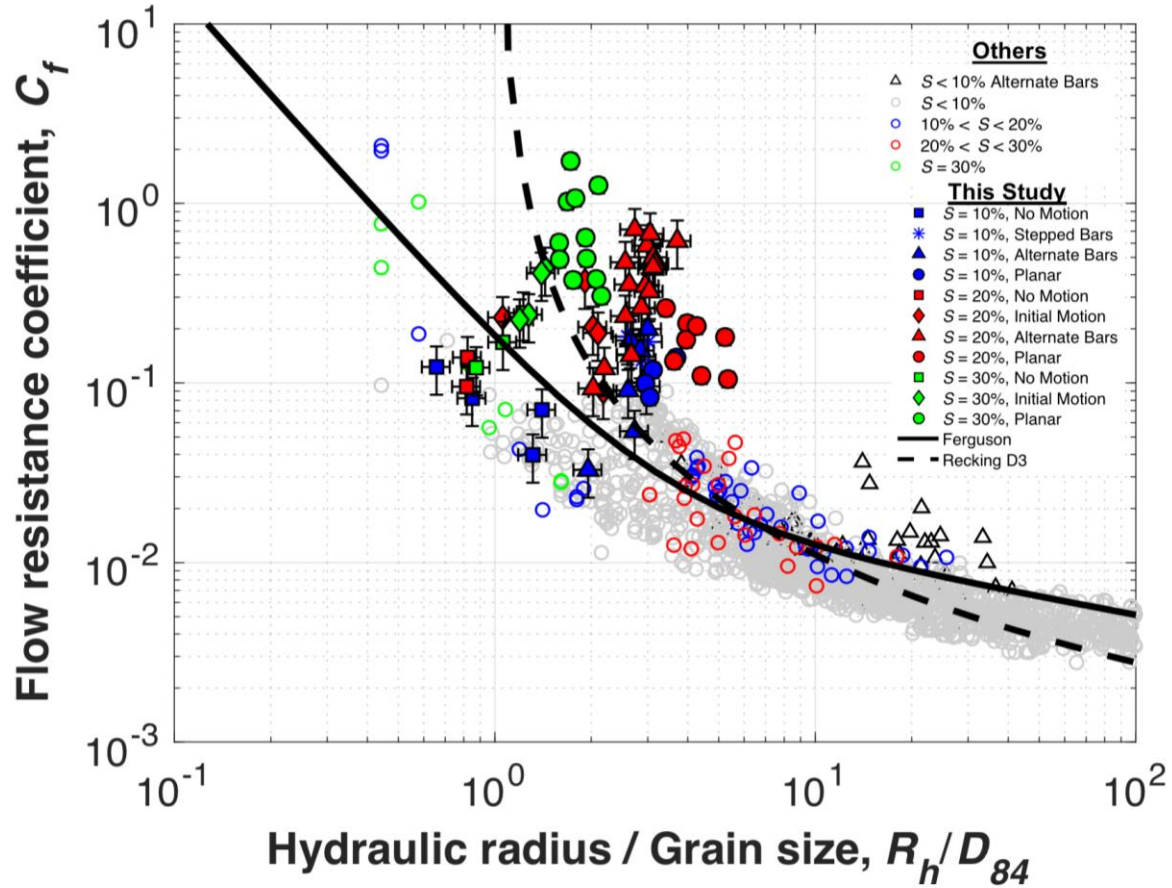
Figure 9. Total flow resistance coefficient, C_f, plotted as a function of R_h/D_{84}. The grey open circles are from previous flume experiments for $S<10\%$ (Bathurst et al., 1984; Ikeda, 1984; Recking, 2006; Lamb et al., 2017a), while the open blue, red, and green circles are from Lamb et al. (2017b) and Bathurst et al. (1984) at $S=10\%$, 20%, and 30% respectively. Data from these flume experiments are shown with filled blue, red, and green markers for $S=10\%$, 20%, and 30%, respectively. Squares are for no motion cases, diamonds are for initial motion cases, triangles are for alternate bar cases, and circles are for planar beds. These data are compared to the Ferguson (2007) variable power equation (VPE), and the Recking et al. (2008) model for flows with high sediment transport stages (their domain 3, *D3*). Error bars represent the relative error.
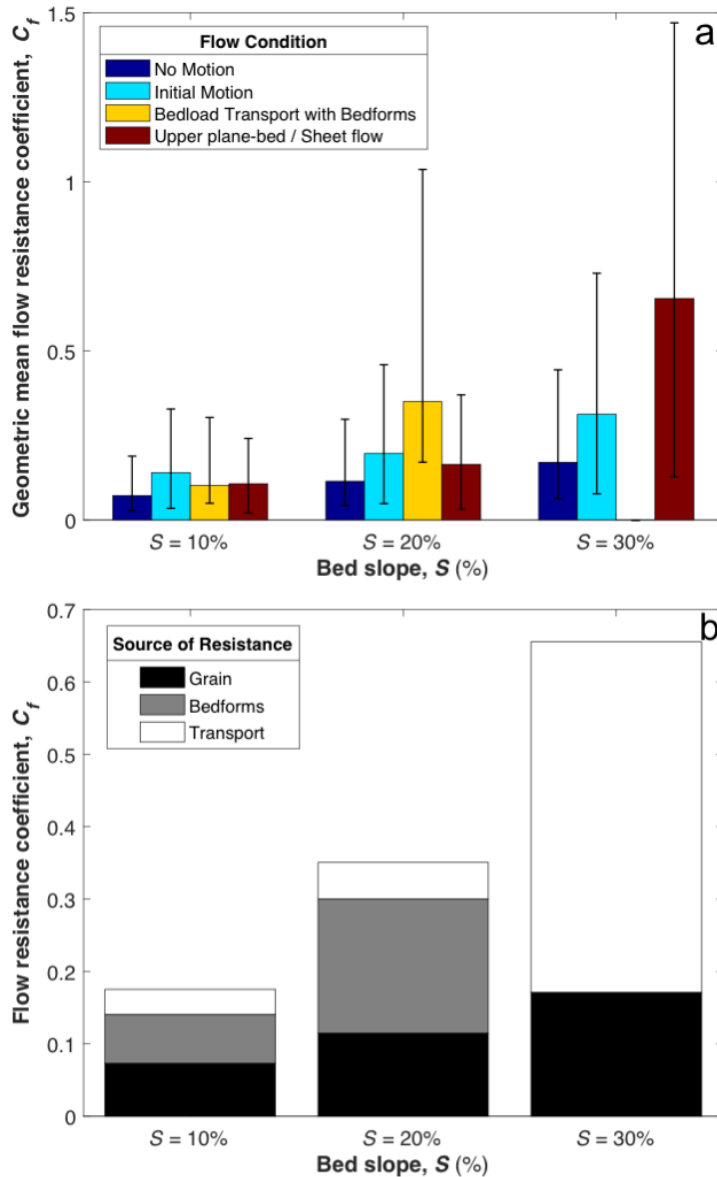
Figure 10. Bar plots showing (a) the geometric mean (and geometric standard deviation as error bars) of the total flow resistance coefficient (C_f) as a function of channel bed slope for cases with different bed states and sediment transport conditions, and (b) contributions of flow resistance for S=10% and S=20% for the cases where sediment transport and bedforms were present, and for S=30% when planar beds with sheetflow occurred. The contributions were determined by linear stress partitioning where the grain component is from no-motion cases.
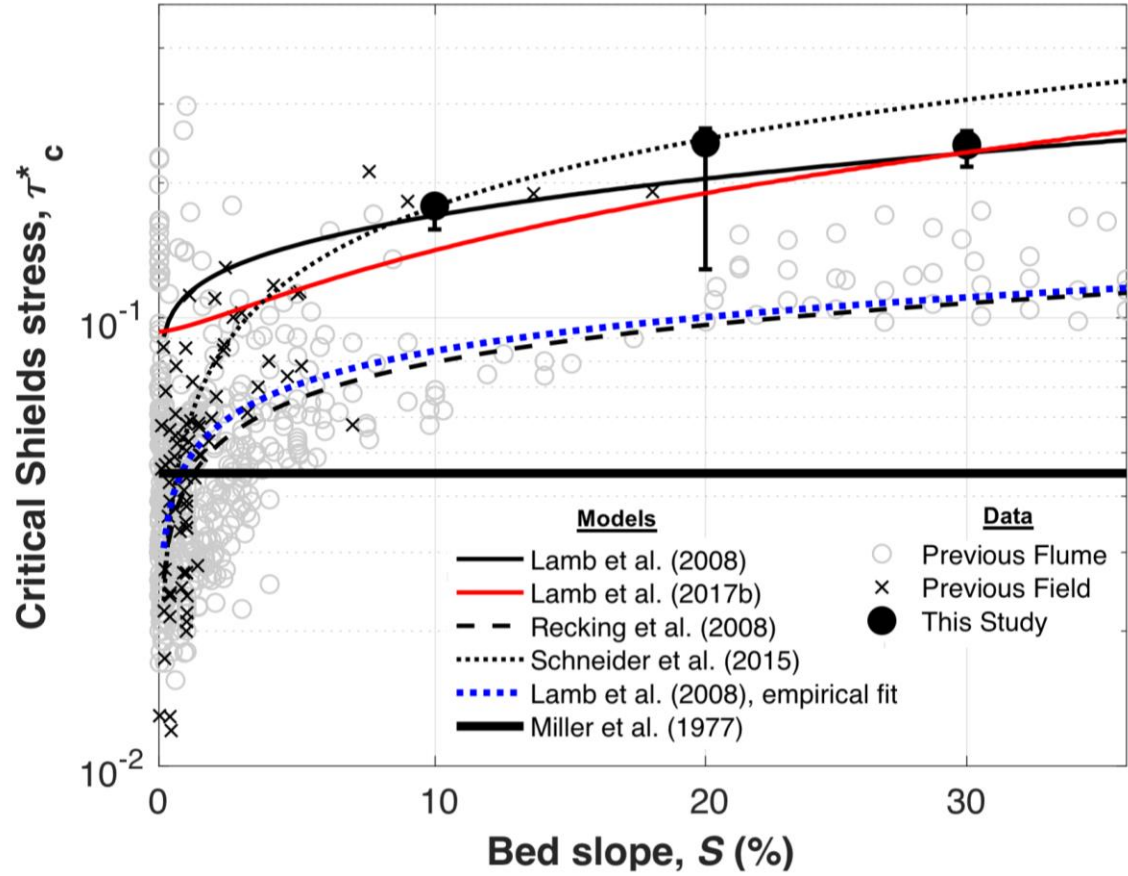
Figure 11. The critical Shields stress as a function of bed slope, where filled circles indicate the median critical Shields stress and the error bars show the data ranges. Flume and field data from previous studies was compiled by Prancevic et al. (2014). For the Lamb et al. (2008) model we use $\phi_o = 62^o$, $\tau_m/\tau_T = 0.7$, $D/k_s = 1$, and $F_L/F_D = 0.85$; for the Lamb et al. (2017) model, $u_o/u^* = 1.5$, $\phi_o = 62^o$, $\tau_m/\tau_T = 0.7$, $D/k_s = 1$, $C_{Lsub} = 1$ and $C_{Dsub} = 0.4$.
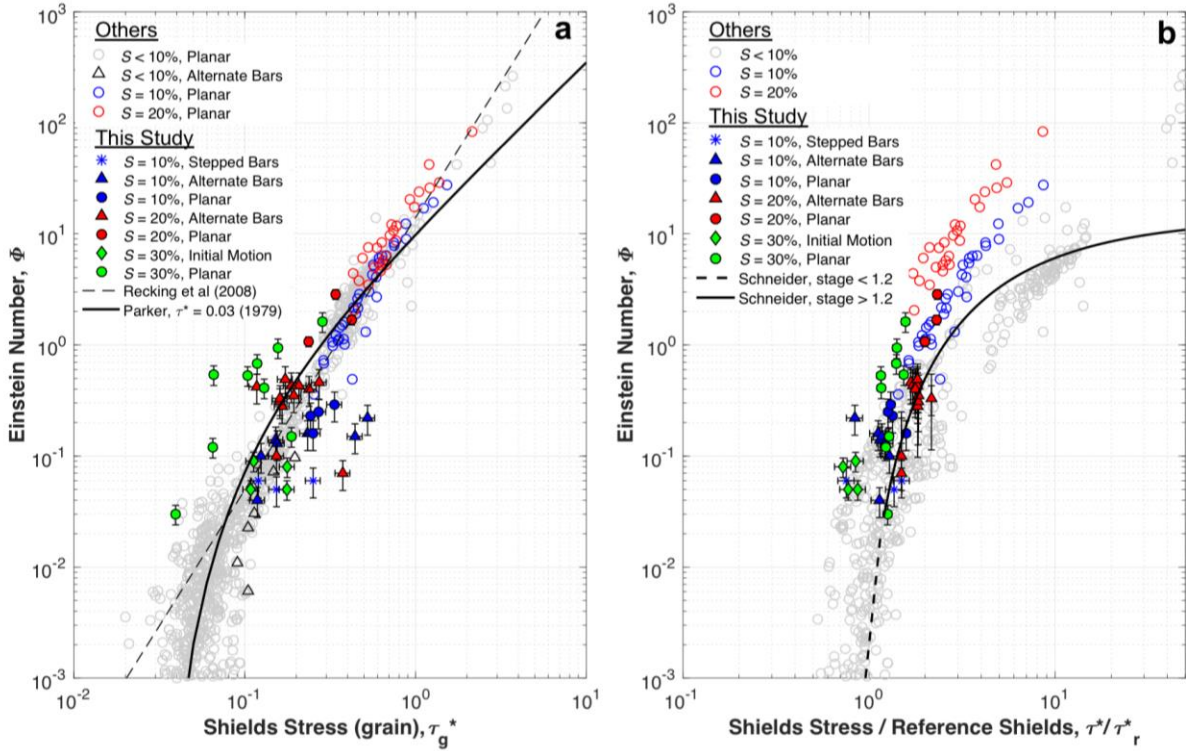
Figure 12. (a) Non-dimensional sediment flux (Φ) as a function of the grain Shields stress (corrected for morphologic drag and sediment transport). The grey open circles are from previous flume experiments for $S<10\%$ (Bathurst et al., 1984; Ikeda, 1984; Recking, 2006), while the open red and blue circles are from Bathurst et al. (1984) at $S=10\%$ and 20%, respectively. Data from these experiments are shown with filled blue, red, and green markers for $S=10\%$, 20%, and 30% respectively. Diamonds are for initial motion cases, triangles are for alternate bar cases, and circles are for planar beds. These data are compared to the Parker (1979) model, which has a constant reference critical Shields stress (i.e., $\tau_c^* = 0.03$), and the Recking (2008) model. (b) Φ as a function of the transport stage, where Shields stress in this case is the total Shields stress (no partitioning) and the reference Shields stress is from Schneider et al. (2015). The data are labeled in the same format as in (a). These data are compared to the

Schneider et al. (2015) transport model, which was developed using data from steep, natural streams with $S \leq 11\%$ and $D > 4$ mm. Error bars represent the relative error.
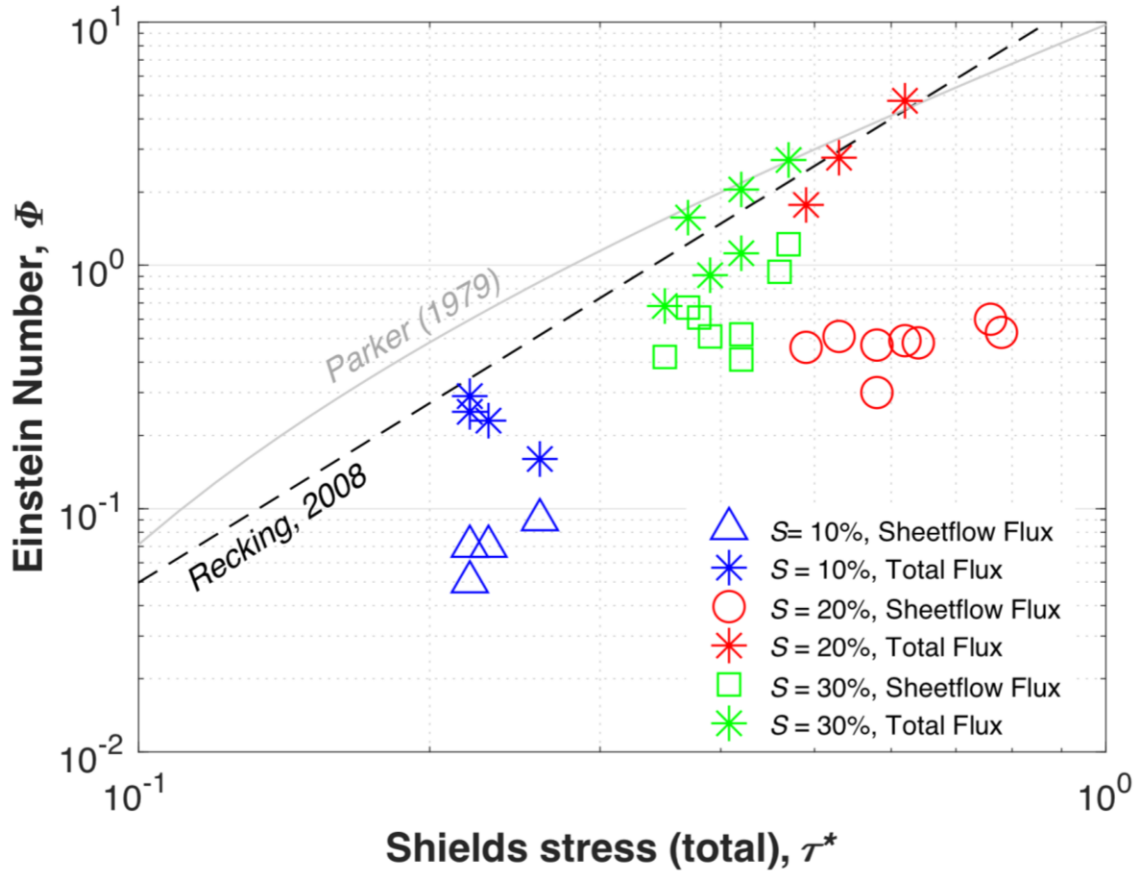

Figure 13. Non-dimensional sediment flux or Einstein number (Φ) versus total Shields stress (τ^*). The black dashed line represents the model proposed by Recking (2008) and the grey line is the relation from Parker (1979). All data for S=10% are shown in blue, S=20% are shown in red, and S=30% are shown in green. Hollow markers indicate sheetflow sediment fluxes estimated from displacement maps (using Eq. (5)) and stars are for total sediment fluxes (bedload + sheetflow) measured in a sediment trap. On average, sheetflow within the bed contributes ~15% of the total measured flux at S=20% and ~44% at S=30%. Errors are within the size the symbol.
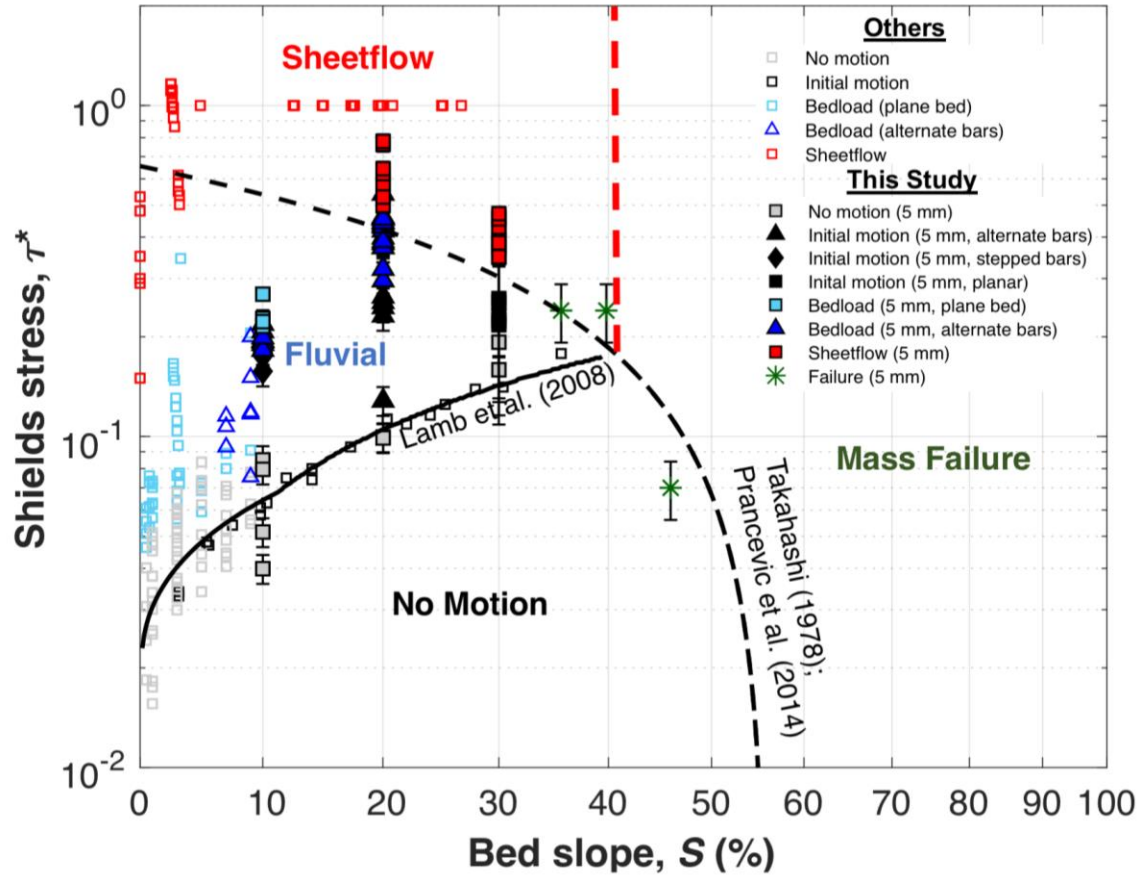
Figure 14. Zones of sediment transport mode following Prancevic et al., 2014 with our data (filled markers) and experimental data from Mizuyama (1977), Bathurst et al. (1984), Asano (1992), Gao (2008), and Prancevic et al. (2014) shown in open markers. Squares indicate a planar bed, triangles indicate alternate bars, and diamonds are stepped-bars (at S=10%). Grey indicates no motion, black indicates initial motion, blue indicates fluvial bedload transport (light blue = planar bed and dark blue = alternate bars), green indicates mass failure, and red indicates sheetflow. The fluvial to debris flow transition as predicted by the Takahashi (1978) bed failure model is shown with the black dashed line, and the Lamb et al. (2008) model for fluvial initial sediment motion is shown with a solid black line. The red dashed line indicates the critical slope, S_c, for the gravels used in these experiments, beyond which mass failure of the bed occurs before fluvial sediment transport (Prancevic et al., 2014). Error bars represent the relative error.

Table 1.

Bed Slope S	Bed State	Shields Stress τ^*	Relative Submergence H / D_{84}	Einstein Number Φ
0.1	No motion (planar)	0.04 – 0.09	0.6 – 1.2	0
0.1	Stepped alternate bars	0.16 – 0.18	2.6 – 3.2	0.05 – 0.06
0.1	Alternate bars	0.14 – 0.22	2.4 – 3.6	0.04 – 0.22
0.1	Upper plane bed	0.22 – 0.26	3.2 – 4.0	0.2 – 0.3
0.2	No motion (planar)	0.1	0.7	0
0.2	Initial motion (non-planar)	0.13 – 0.26	0.9 – 2.2	0
0.2	Alternate bars	0.3 – 0.5	2.4 – 4.6	0.1 – 0.5
0.2	Upper plane bed, sheetflow	0.49 – 0.78	3.5 – 5.8	1.1 – 2.9
0.3	No motion (planar)	0.16 – 0.22	0.7 – 1.0	0
0.3	Initial motion (planar)	0.22 – 0.26	1.1 – 1.2	0.05 – 0.09
0.3	Upper plane bed, sheetflow	0.35 – 0.47	1.6 – 2.2	0.03 – 1.6